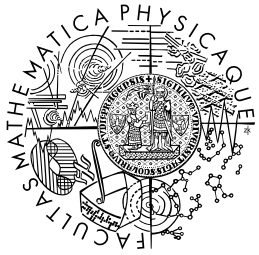

FACULTY
OF MATHEMATICS
AND PHYSICS
Charles University

MASTER THESIS

Martin Kihoulou

Impact crater relaxation throughout the Solar System

Department of Geophysics

Supervisor of the master thesis: RNDr. Klára Kalousová, Ph.D.
Study programme: Physics
Study branch: Geophysics

Prague 2021

I declare that I carried out this master thesis independently, and only with the cited sources, literature and other professional sources. It has not been used to obtain another or the same degree.

I understand that my work relates to the rights and obligations under the Act No. 121/2000 Sb., the Copyright Act, as amended, in particular the fact that the Charles University has the right to conclude a license agreement on the use of this work as a school work pursuant to Section 60 subsection 1 of the Copyright Act.

In ..... date ....

Author's signature

In this place I would like to thank my supervisor RNDr. Klára Kalousová, Ph.D., for her inspiring guidance and carefulness. Equally, I am grateful to RNDr. Ondřej Souček, Ph.D., for his help with the implementation of spherical axisymmetry in FEniCS software, to prof. RNDr. Ondřej Čadek, CSc., for his wise and illuminating ideas, and to RNDr. Ladislav Hanyk, Ph.D., for showing me magick tricks. Special thanks goes to my dearest Bára.

The financial support by the Czech Science Foundation Project 19-10809S, SVV-260581 and Grant Agency of Charles University Project 111-10/251851 is highly acknowledged.

Title: Impact crater relaxation throughout the Solar System

Author: Martin Kihoulou

Department: Department of Geophysics

Supervisor: RNDr. Klára Kalousová, Ph.D., Department of Geophysics

Abstract: In this thesis, we study the viscous relaxation of an impact-deformed icy shell of a dwarf planet Pluto. Motivation for this work is the position of Sputnik Planitia, a 1000 km wide, nitrogen-filled elliptic basin, which is located very close to Pluto-Charon tidal axis. Given this unlikely position on Pluto's surface, it was suggested that the basin was formed elsewhere and the whole body reoriented afterwards. For the reorientation to occur, the basin has to generate a positive gravity anomaly for which a combination of impact-related subsurface ocean uplift, ejecta blanket and accumulation of nitrogen ice was suggested. However, to maintain the orientation towards the minimum principal axis of inertia until today, the ocean uplift must be present on timescales of billions of years, which may be achieved due to an insulating layer of high viscosity clathrates at the ice/ocean interface. We solve Pluto's ice shell evolution by the finite element method in 2D spherical axisymmetric geometry with an evolving free surface and assuming a viscous rheology. Our results show that the thermal effect of the impact and nonlinear rheology can substantially decrease the relaxation timescale. It thus seems unlikely that the uplift would be stable long enough, even if the clathrates are present.

Keywords: Pluto, viscous deformation, crater relaxation, axisymmetric geometry

Název práce: Relaxace impaktních kráterů ve sluneční soustavě

Autor: Martin Kihoulou

Katedra: Katedra geofyziky

Vedoucí práce: RNDr. Klára Kalousová, Ph.D., Katedra geofyziky

Abstrakt: V této práci studujeme viskózní relaxaci impaktem deformované ledové slupky trpasličí planety Pluto. Motivací je poloha eliptické, 1000 km široké pánve Sputnik Planitia, která se nachází v těsné blízkosti slapové osy. Vzhledem k její neobvyklé poloze se usuzuje, že pánev vznikla jinde a k přiblížení ke slapové ose došlo reorientací celého tělesa. Aby k reorientaci tímto směrem mohlo dojít, musí mít gravitační anomálie oblasti pánve kladné znaménko. Jedná-li se o impaktní pánev, lze jej docílit izostatickým výzdvihem podpovrchového oceánu, impaktními ejekty a naakumulovaným volatilním dusíkem. Aby si pánev novou polohu ve směru nejmenšího hlavního momentu setrvačnosti zachovala dodnes, výzdvih oceánu musí být přítomen řádově miliardy let. Tomu by mohla pomoci izolační vrstva vysokoviskózních klatrátů na rozhraní oceánu a ledu. Deformaci ledové slupky řešíme metodou konečných prvků ve 2D sférické axisymetrické geometrii s volným povrchem a viskózní reologií. Naše výsledky ukazují, že termální účinek impaktu a nelineární reologie dokáží výrazně urychlit charakteristický čas relaxace. Zdá se tedy, že navzdory přítomnosti klatrátů výzdvih oceánu nebude stabilní dostatečně dlouho.

Klíčová slova: Pluto, viskózní deformace, relaxace kráterů, axisymetrická geometrie

Contents

Introduction

Impact craters were present, at least for some period of time, on all solid surfaces in the Solar System. If not destroyed by tectonic processes, they can now be found on all terrestrial planets, satellites and on other, mostly airless, bodies. Since impact cratering is for most of these bodies the dominant geological process, we can obtain valuable information about the body geological history from impact crater morphology [Melosh, 2011]. However, the impact does not affect the surface only. Numerical simulations suggest that a collision with another body can bring significant changes also to the target body interior. If a fluid or low viscosity mantle is present beneath a rigid lithosphere, isostatic uplift of the mantle may occur below the place of the impact. The resulting gravity anomaly may even lead to whole body reorientation (true polar wander) [Johnson et al., 2016, Nimmo et al., 2016a].

Nimmo et al. [2016a] proposed that this might be the case of a dwarf planet Pluto. Sputnik Planitia, a 1000 km wide, nitrogen-filled elliptic basin on its surface, is situated only 400 km from the tidal axis. Since a position this close to the tidal axis is very unlikely, Nimmo et al. [2016a] proposed that the whole body was reoriented. To reorient towards the tidal axis, which is the minimum principal axis of inertia, Sputnik Planitia should be a positive gravity anomaly. Based on its possible impact origin, isostatic uplift of the water mantle might have compensated the basin's negative topography. Ejecta blanket and accumulated nitrogen would then provide an additional positive mass which would reorient the whole body [Keane et al., 2016]. Due to the basin's likely age of ~ 4 Gyr [Greenstreet et al., 2015], the gravity anomaly has to be positive up to the present, i.e.. the uplift should relax extremely slowly. Since the warm ice close to the melting point is expected to relax quickly, Kamata et al. [2019] proposed the presence of an insulating layer of high viscosity clathrates, which should prolong the relaxation time of the uplift.

In this thesis, we will investigate the viscous relaxation of Sputnik Planitia basin and its uplift. In Chapter 1, we summarize the basic knowledge about the dwarf planet Pluto and discuss the hypotheses of Sputnik Planitia's origin and possible reorientation. Chapter 2 provides a brief description of crater formation, its morphology and the parametrization of the thermal and topographic effects of an impact. In Chapter 3, we develop the mathematical description of a viscous flow in an icy shell with free boundary. We solve the problem by the finite element method and we present several numerical tests to verify our implementation. In Chapter 4, the material properties of ice are discussed and results for surface crater and uplift relaxation are presented. Finally, the results and further objectives are discussed.

The potential presence of a liquid ocean beneath the outer shells of icy bodies is currently on the front burner of planetary research, since liquid water is one of the necessary conditions for the emergence of life as we know it. There is already a serious evidence for several icy moons: induced magnetic field in case of Europa and Ganymede, geysers at Enceladus or Titan's obliquity [Nimmo and Pappalardo, 2016]. Due to Pluto's likely origin in the Kuiper belt, there are probably many other bodies with a similar interior structure. For this reason,

answering the question of subsurface ocean presence is crucial for further research.

Unfortunately, future exploration of Pluto remains unclear. Pluto orbiter or lander is considered as a possible mission, however, it will not be launched before 2030. Until then, numerical modelling of geological processes may bring new knowledge about this beautiful and enigmatic world.

1. Pluto and Sputnik Planitia

At the beginning of the 20th century, American astronomer Percival Lowell, later director of Lowell Observatory, searched for Planet X that caused an anomaly in Uranus's orbit. Based on his calculations, astronomer Clyde Tombaugh in 1930 at the same observatory discovered Pluto. Although it was not the Planet X that he searched for[1], it was the last member of family of planets (at that time) of Solar System. It orbits the Sun at an average distance of 40 AU with great eccentricity $e = 0.246$ and great inclination to ecliptics $i = 17.16°$.

1.1 Pluto as an icy body

With an orbital period of 248 years, Pluto did not have enough time to complete a single orbit since its discovery. Nevertheless, thanks to Hubble Space Telescope, we were able to observe its surface. Figure 1.1 shows surface changes between years 1994 and 2002/2003 [Stern et al., 2010]. At the latter photography, a hemispherical pattern, probably caused by summer approaching at the northern hemisphere, is clearly visible. Possible volatiles might sublime and refreeze in the colder southern region of Pluto.

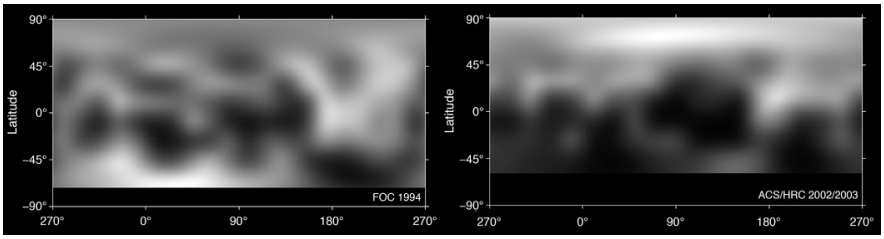

Figure 1.1: Pluto's surface as viewed by Hubble Space Telescope in 1994 (left) and 2002/2003 (right). Visible surface changes are probably a consequence of volatiles sublimation [Stern et al., 2010].

In 2015 New Horizons Spacecraft performed a flyby of Pluto and Charon and gave us valuable information about these two bodies including high-resolution images of their surfaces (see Figure 1.2) or surface chemical composition. The surface of Pluto is made up of water ice, nitrogen, carbon oxide and methane [Grundy et al., 2016]. Due to extremely low temperature ($\approx$ 40 K), all these components are in solid state. Despite that, Pluto is geologically active. Owing to high tilt and eccentricity, there are seasonal variations of surface temperature which lead to (de)sublimation of volatile compounds. There are also regions of glacier flow of solid nitrogen similar to that of water ice observed on Earth. From geological point of view, there is a high number of impact craters (indicating old age of the surface), extensional fractures and normal faults (indicating despinning and expansion [Matsuyama and Nimmo, 2013]), or bladed terrains formed by sublimation, so far unique in the Solar System [Moore et al., 2016].

[1] In 1992, Neptune's mass was recalculated from flyby data of Voyager 2 spacecraft. The mass difference 0.5 % from the previous estimate showed that there was no perturbation of Uranus's orbit and therefore no need for Planet X [Standish, 1993]. However, this topic has been revived recently by Batygin and Brown [2016].

The dominant feature on Pluto's surface is a large elliptical basin informally named Sputnik Planitia. It is 1200× 900 km wide and covered by a layer of convecting nitrogen ice, which makes it impossible to observe its depth directly. However, it is possible to estimate the nitrogen ice thickness from dimensions of the convecting cells. It is now argued that its thickness varies from 3 to 10 km [Trowbridge et al., 2016]. Absence of impact craters indicates that the surface of Sputnik Planitia is not older than 10 Myr. Based on the sublimation pits in the convection cells, Buhler and Ingersoll [2017] suggested that the surface is approximately 140 - 270 kyr.

Figure 1.2: Pluto with Sputnik Planitia in the middle imaged by New Horizons spacecraft in 2015 [NASA, 2018].

Pluto is in a synchronous rotation with its biggest satellite Charon. Since Charon weights 12 % of Pluto's mass, their barycentre lays outside Pluto. Sputnik Planitia basin lays interestingly almost at the anti-Charon point (its centre is only 400 km from the tidal axis, see Figure 1.3). Nimmo et al. [2016a] and Keane et al. [2016] argue that the crater center has a $5 - 9$ % chance to be this close to the tidal axis. Nimmo et al. [2016a] proposed that Sputnik Planitia is an impact basin which was formed somewhere else and that it was subsequently reoriented. In the next section, we will discuss the different theories for the reorientation of Sputnik Planitia basin and their requirements and consequences.

1.2 Origin and current position of the basin

If Pluto was reoriented, Sputnik Planitia basin has to be a positive gravity anomaly. So far two main theories explaining possibles source of this anomaly were proposed.

Nitrogen glacier theory

Hamilton et al. [2016] showed that nitrogen ice caps can be rapidly accumulated near lattitudes of $\leq 30°$. These areas are, averaged over orbital period, the coldest ones. Since nitrogen ice has a high albedo, these areas reflect the majority

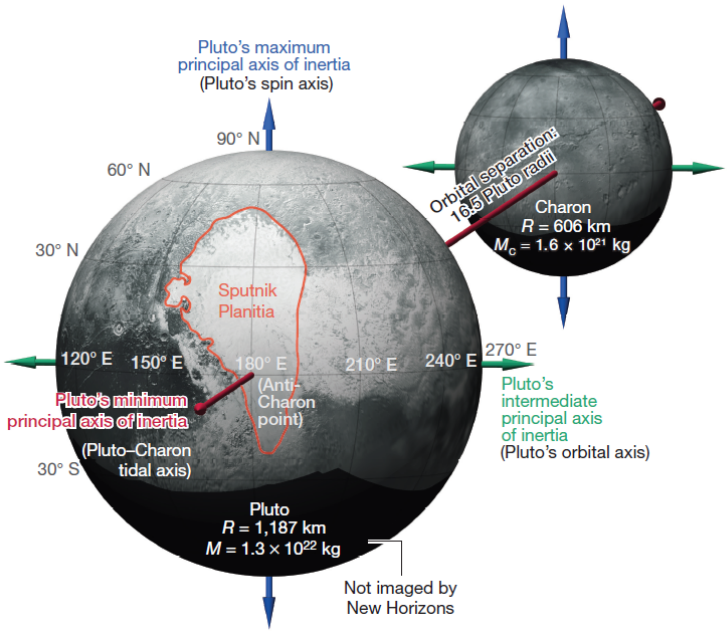

Figure 1.3: Position of Sputnik Planitia basin with respect to Pluto-Charon tidal axis [Keane et al., 2016].

of sunlight and remain cold, while other darker areas absorb it and warm up (this principle is also called *runaway albedo effect*). However, for only one cap to survive, many processes have to be involved (e.g. eccentricity of Pluto's orbit or continuous illumination of only one hemisphere of Pluto by Charon). Accumulation of nitrogen ice in one cap leads to a positive gravity anomaly which reorients this cap to anti-Charon point. Over geological timescales, the nitrogen cap subsides, creating the Sputnik Planitia basin. Meanwhile, on timescales of hundreds Myr, Pluto and Charon become tidally locked, raising a permanent tidal bulge [Robuchon and Nimmo, 2011]. This tidal bulge prevents further reorientation even if the glacier, already subsided, does not generate positive gravity.

However, this scenario is not likely, because Nimmo et al. [2016b] shows that there is no tidal bulge on both Pluto or Charon. Absence of these features suggests that at the moment when the despinning was finished, the bodies were still too warm and deformable. Without the proposed tidal bulge, Pluto would reorient to another minimum energy configuration at the moment of ice cap subsidence.

Impact basin theory

Nimmo et al. [2016a] proposed that Sputnik Planitia basin is a result of an impact. The impact basin itself, however, produces a negative gravity anomaly, unless it is compensated. If the surface basin was compensated by mantle (ocean) uplift, the accumulated nitrogen would contribute to the positive gravity anomaly required for reorientation.

Numerical simulations of the impact suggest that the ocean uplift would not be sufficient to compensate the crater negative anomaly completely [Johnson et al., 2016, Denton et al., 2020], unless the ocean has higher density (at least 1100 kg $\cdot$ m^3). This might be achieved e.g. by dissolved $MgSO_4$, see Section 4.2.1. However, Keane et al. [2016] show that ejecta blanket can also contribute

to positive gravity anomaly, therefore the uplift does not have to be fully isostatic to cause reorientation.

Assumption of the ocean uplift requires a liquid ocean beneath the ice shell at the time of an impact. There are already several indications for the presence of a liquid ocean at the time of an impact:

1. Energy balance of radioactive decay, accretion energy, despinning and differentiation suggest that Pluto might have developed a subsurface ocean only if the ice at melting temperature is sufficiently viscous (reference viscosity $\geq 4 \cdot 10^{15}$ Pa $\cdot$ s). Convection then becomes sluggish or entirely absent, thus the ocean looses heat sufficiently slowly to remain liquid up to the present. [Robuchon and Nimmo, 2011].

2. Extensional faults observed on Pluto's surface suggesting volume increase are best explained by freezing of a liquid ocean [Keane et al., 2016, Bierson et al., 2020].

3. Existence of an ocean is in agreement with the absence of a fossil bulge [Nimmo et al., 2016b].

4. On the opposite side of Sputnik Planitia (i.e. sub-Charon point), the *antipodal terrain* resembles the *weird terrains* on the Moon or Mercury (see Section 2). They are believed to be caused by elastic waves generated by an impact on the opposite side of the body (Sputnik Planitia basin on Pluto, Imbrium or Orientale basins on the Moon). Simulations for Pluto show that antipodal deformation is sensitive to ocean thickness. Best results were obtained for a 150 km thick ocean [Denton et al., 2020].

Since there is no fossil bulge, the gravity anomaly has to be positive up to the present. This is nearly impossible to satisfy because the low ice viscosity at melting temperature causes the uplift to relax very quickly. Nimmo et al. [2016a] thus proposed an extremely cold ocean, whose freezing point (190 K) would have been lowered by dissolved ammonia. Even though ammonia lowers the freezing point, it also reduces water density, which makes the uplift gravity contribution insufficient for reorientation. Kamata et al. [2019] proposed presence of a clathrate hydrate layer at the bottom of the ice shell to prolong the relaxation time of an ocean uplift. Clathrates have higher viscosity than water ice and low thermal conductivity which makes the shell cooler and more rigid [Durham et al., 2003]. This thermal and mechanical effect will be discussed in Section 4.2.

2. Impact cratering

Although impact craters have accompanied Solar System bodies since the first solid surface was formed, they were discovered only 400 years ago, when Galileo Galilei pointed his telescope at the Moon. Still, the origin of circular-shaped features remained unknown until 1930. Before impact physics was developed, impact craters on the Moon were believed to be extinct volcanoes. However, impact character of Moon's features was not proved until high-resolution images and Apollo missions in the 1970s. Since then, impact craters were discovered on most of the bodies of Solar System.

2.1 Impact mechanism

Impact craters can provide us with useful information about both surface and inner processes. From crater counting we can decide about relative age of surface regions. On the one hand, there are bodies with almost no impact craters (e.g. icy moon Europa or the south pole of Enceladus), whose smooth surface is a sign of ongoing or recent resurfacing processes implying rich sources of internal energy. On the other hand, heavily cratered bodies like planet Mercury, the Moon or icy moon Callisto are likely inactive for a very long time [Melosh, 2011].

The birth of a crater is a very complex process. It starts with contact and compression, when an impactor (typically an icy or rocky body) compresses the target's surface. This stage lasts only on short timescales of the order of d/v_{imp}, where d is impactor diameter and v_{imp} impact velocity (usually few - tens km$\cdot$s^{-1}). Depending on the impact velocity and elastic velocities of the impactor and the target, a shock wave may travel through both objects. At the end of this stage, the impactor/target interface is less than one impactor diameter below the original target surface and both impactor and surrounding target can be already melted or vaporized. Amount of vaporized material can be even sufficient to form an upwelling plume that can reach escape velocity and leave the target, removing part of the original atmosphere.

After the material is compressed, it gets ejected and the crater is opening. This stage is called an excavation and the resulting crater *a transient crater*. The opening timescale is given by $\sqrt{D/g}$, where D is the crater diameter and g the target's surface gravity. Furthermore, shock wave slows down and propagates further as an elastic wave. It might even travel to the body antipode to meet with the wave from the opposite direction and form so-called *weird terrains*. This was confirmed for the antipodal terrains of Imbrium and Orientale craters on the Moon or Caloris Basin on Mercury (see Figure 2.1). It might be also the case of antipodal terrains of Pluto's vast basin Sputnik Planitia [Denton et al., 2020].

The last stage of crater formation is *modification*. Transient crater walls are collapsing and floor establishes its final depth and shape. At this moment, we distinguish between bowl-shaped *simple* craters and more complicated *complex* craters, that might form a central peak or a peak ring. Transition radius between simple and complex craters depends on the body material and scales as g^{-1}. Typical transition radii are 3 km for Earth while 20 km for Moon. Special category of complex craters are *multiring craters* (found e.g. on the Moon, Ganymede

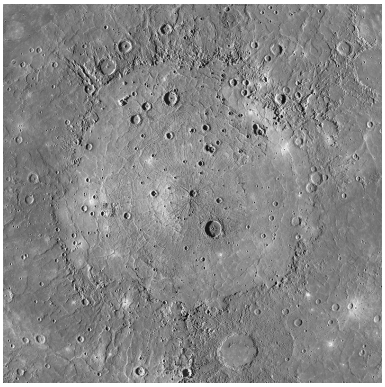

(a) Caloris basin on Mercury.

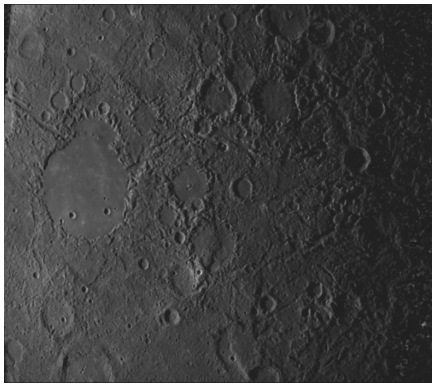

(b) Antipode of Caloris basin.

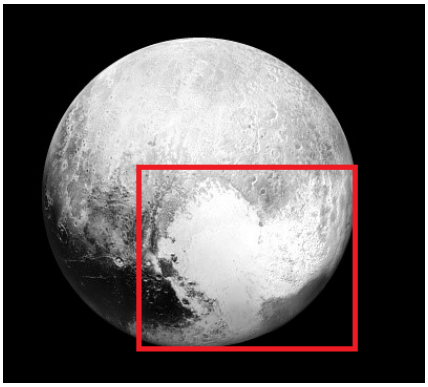

(c) Sputnik Planitia basin on Pluto.

(d) Antipode of Sputnik Planitia basin.

Figure 2.1: **(a)** Caloris basin (diameter 1350 km) on Mercury [NASA/JPL/Northwestern University, 2015], **(b)** its antipodal terrain (800 × 800 km window). **(c,d)** Sputnik Planitia basin (diameter 1000 km) on Pluto and its antipodal terrain [NASA/JHUAPL/SwRI, 2015].

or Calisto), which are one of the very largest impact features in Solar System. After the modification is over, slower processes such as isostatic adjustment or relaxation, commence [Melosh, 2011].

2.2 Thermal and topographic effects

When the impactor hits the target, part of its kinetic energy is transformed into inner energy (local increase of temperature of target). If the impact velocity is larger than the elastic velocities of the target, a shock wave develops. Shock pressure, associated with shock wave, is nearly uniform in a spherical region beneath the impact (the *isobaric core*) and strongly decays away from it (see Figure 2.2).

Based on energy balance calculations and shock simulations, the radius of an isobaric core R_{ic} is slightly larger than the radius of the impactor R_{imp} [Monteux et al., 2014]

$$R_{\mathrm{ic}} = \sqrt[3]{3} R_{\mathrm{imp}}. \tag{2.1}$$

Inside the isobaric core ($r < R_{\mathrm{ic}}$), the thermal increase ΔT is uniform,

$$T(r) = T_0 + \Delta T, \tag{2.2}$$

where T_0 is the pre-impact temperature, r is the distance from the centre of the isobaric core, while for distances r larger than isobaric core radius R_{ic}, it decays as

$$T(r) = T_0 + \Delta T \left(\frac{R_{\text{ic}}}{r} \right)^m, \tag{2.3}$$

where m is an attenuation exponent with approximate value $m \approx 3.4$ [Monteux et al., 2007].

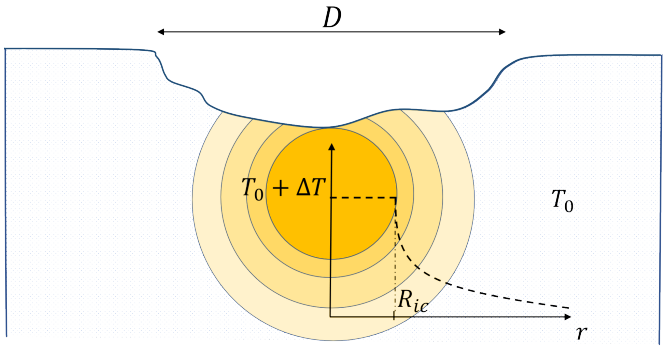

Figure 2.2: Temperature anomaly. For $r \leq R_{\text{ic}}$ the temperature anomaly is constant, for $r > R_{\text{ic}}$ it decreases with increasing r. D denotes the final crater diameter.

Denoting γ a fraction of an impactor kinetic energy E_k dissipated as a heat, we can estimate the temperature increase as

$$\Delta T = \gamma \frac{E_k}{\rho c_p V_{\text{eff}}}, \tag{2.4}$$

where ρ and c_p are density and specific heat capacity of target, respectively, and V_{eff} is the effective volume which is considered to be heated. It can be related to the volume of the isobaric core

$$V_{\text{eff}} = h_m V_{\text{ic}}, \tag{2.5}$$

with $h_m = 5.8$ [Monteux et al., 2007].

Using Equations (2.1) and (2.5), we can express the effective volume in terms of the impactor volume

$$V_{\text{eff}} = 3 h_m V_{\text{imp}}, \tag{2.6}$$

and thus for temperature anomaly we have

$$\Delta T = \gamma \frac{1}{2} \frac{\rho_{imp} V_{\text{imp}} v_{\text{imp}}^2}{\rho c_p 3 h_m V_{\text{imp}}} = \frac{1}{6} \frac{\rho_{\text{imp}} v_{\text{imp}}^2}{\rho c_p h_m} \gamma. \tag{2.7}$$

It is also possible to formulate a scaling law for the final crater diameter

$$D = a_0 \left(\frac{v_{\text{imp}}}{v_{\text{esc}}} \right)^{2a_1} \left(\frac{\rho_{\text{imp}}}{\rho} \right)^{a_2} R^{a_3} d_{\text{imp}}^{a_4} \cos^{a_5}(\theta), \tag{2.8}$$

where v_{esc} is escape velocity, R is the target radius, d_{imp} is the impactor diameter and θ is impact angle. The values of parameters a_i are as follows: $a_0 = 1.1$, $a_1 = 0.217$, $a_2 = 0.333$, $a_3 = 0.217$, $a_4 = 0.783$, and $a_5 = 0.44$ [Zahnle et al., 2003].

3. Viscous flow in an ice shell with free surface

In this chapter, we will mathematically describe the problem of viscous flow in an ice shell with free surface. In Section 3.1, we formulate the strong form of relaxation-convection problem based on balance laws (for mass, momentum and energy), their boundary conditions and kinematic condition for free surface. ALE method and its consequence is briefly described. Finally, the weak form, implementation and numerical tests of the problem in Cartesian and cylindric geometry are discussed in Sections 3.2 and 3.3, respectively.

3.1 Problem formulation

3.1.1 Governing equations

The problem of viscous flow will be described by following balance laws in Boussinesq approximation [Matyska, 2005].

Mass balance for an incompressible fluid gives

$$0 = \nabla \cdot \boldsymbol{v}, \tag{3.1}$$

where $\boldsymbol{v}$ denotes velocity of the flow.

Momentum balance at geological timescale expresses an equilibrium between hydrostatic pressure, viscous forces and volume forces

$$0 = -\nabla p \boldsymbol{I} + \nabla \cdot \eta(\nabla \boldsymbol{v} + \nabla^T \boldsymbol{v}) + \rho_{\mathrm{i}}(1 - \alpha(T - T_{\mathrm{ref}}))\boldsymbol{g}, \tag{3.2}$$

where p denotes pressure, η viscosity of ice (in general function of temperature, grain size and stress), ρ_i density of ice at reference temperature T_{ref}, α thermal conductivity and $\boldsymbol{g}$ gravity.

Energy balance describes the evolution of temperature caused by conduction of heat and convection of heat

$$\rho_{\mathrm{i}} c_p \frac{\partial T}{\partial t} = \nabla \cdot (k \nabla T) - \rho_{\mathrm{i}} c_p (\boldsymbol{v} \cdot \nabla T), \tag{3.3}$$

where c_p denotes isobaric specific heat, T temperature, t time, k thermal conductivity (in general function of temperature).

Free surface kinematic condition describes evolution of free surface resulting from velocity field

$$\frac{\partial h}{\partial t} = (\nabla h \cdot \boldsymbol{t})(\boldsymbol{v} \cdot \boldsymbol{t}) - \boldsymbol{v} \cdot \boldsymbol{n}, \tag{3.4}$$

where h denotes the height of a free surface, $\boldsymbol{n}$ and $\boldsymbol{t}$ are normal and tangent vectors to the surface, respectively.

3.1.2 Boundary conditions

Let Ω be a domain and Γ its boundary. This boundary can be divided in three disjoint subdomains $\Gamma = \Gamma_{\text{top}} \cup \Gamma_{\text{bottom}} \cup \Gamma_{\perp}$. Subdomains Γ_{top} and Γ_{bottom} represent top and bottom surfaces, respectively, while $\Gamma_{\perp}$ represents vertical surfaces (left/right side for Cartesian geometry, axis of symmetry for spherical geometry).

For temperature, we use Dirichlet boundary condition (fixed temperature) at the top and bottom boundaries and Neumann condition (zero heat flux) elsewhere

$$\begin{aligned} T &= T_{\text{top}} && \text{at } \Gamma_{\text{top}}, \\ T &= T_{\text{bottom}} && \text{at } \Gamma_{\text{bottom}}, \\ \nabla T \cdot \boldsymbol{n} &= 0 && \text{at } \Gamma_{\perp}. \end{aligned} \tag{3.5}$$

For velocity, we will use three types of boundary conditions. The first of them is free-slip, which allows the material to move freely along the boundary

$$\begin{aligned} \boldsymbol{v} \cdot \boldsymbol{n} &= 0 \quad \text{at } \Gamma, \\ (\boldsymbol{\sigma} \cdot \boldsymbol{n})_t &= 0 \quad \text{at } \Gamma, \end{aligned} \tag{3.6}$$

where $\boldsymbol{\sigma}$ denotes deviatoric part of stress tensor $\boldsymbol{\tau}$

$$\boldsymbol{\tau} = -p\boldsymbol{I} + \boldsymbol{\sigma} \tag{3.7}$$

This condition can be prescribed at the solid/fluid (e.g. ice/ocean) interface.

Another possibility is no-slip, which restricts movement at the boundary

$$\boldsymbol{v} = \boldsymbol{0} \quad \text{at } \Gamma, \tag{3.8}$$

which is the case of solid/solid (e.g. ice/rock) interface.

The last boundary condition used is the free boundary, which will be prescribed in case of free surface evolution

$$\boldsymbol{\tau} \cdot \boldsymbol{n} = \boldsymbol{0} \quad \text{at } \Gamma. \tag{3.9}$$

3.1.3 ALE method

Equations summarized in the previous sections are formulated in Eulerian reference frame. This approach is commonly used in fluid mechanics, because physical quantities are associated with fixed spatial points. By contrast, Lagrangian reference frame associates physical quantities with material particles. Therefore, the material points coincide with the same grid points during the whole motion. However, while solving the free surface evolution, we need to deform the computational mesh and describe the fluid motion at the same time.

To achieve this, we will use Arbitrary Lagrangian-Eulerian (ALE) method which is based on an introduction of a mesh (or computational) referential frame, different from both Eulerian and Lagrangian frames [Scovazzi and Hughes, 2007, Donea et al., 2004]. The main advantage of this approach is that the mesh reference frame is not fixed to material or spatial points, but takes into consideration convective effects.

Let us consider Lagrangian Ω_X, Eulerian Ω_x and mesh Ω_χ references frame with position vectors $\boldsymbol{X}$, $\boldsymbol{x}$ and $\boldsymbol{\chi}$, respectively (see Figure 3.1).

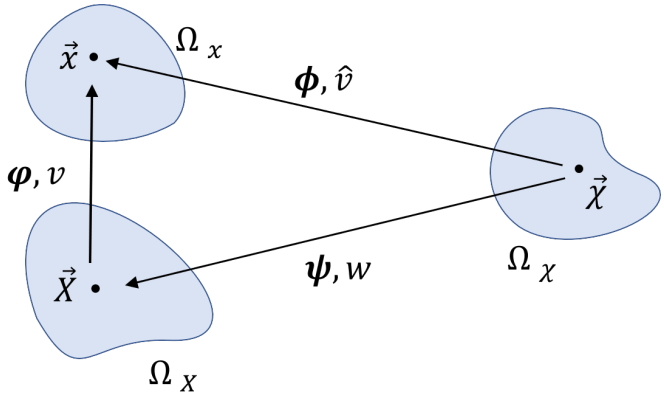

Figure 3.1: Mappings and velocities between the Lagrangian (left bottom), Eulerian (left top) and the mesh reference frame (right).

Let $\alpha(\boldsymbol{x}, t)$ be an arbitrary scalar function in Eulerian reference frame. Velocities $\boldsymbol{v}$ and $\hat{\boldsymbol{v}}$ denote velocity of material particle $\boldsymbol{X}$ and velocity of a mesh node $\boldsymbol{\chi}$ in the spatial (Eulerian) reference frame, respectively. We want to relate the material and mesh time derivatives of $\alpha(\boldsymbol{x}, t)$ with spatial gradient of $\alpha(\boldsymbol{x}, t)$. It will hold

$$\left.\frac{\partial \alpha(\boldsymbol{x}, t)}{\partial t}\right|_{\boldsymbol{X}} = \left.\frac{\partial \alpha}{\partial t}\right|_{\boldsymbol{\chi}} + \boldsymbol{v} \cdot \nabla_{\boldsymbol{x}} \alpha - \hat{\boldsymbol{v}} \cdot \nabla_{\boldsymbol{x}} \alpha, \tag{3.10}$$

where $\nabla_{\boldsymbol{x}} = \partial / \partial \boldsymbol{x}$ denotes the gradient with respect to spatial coordinate (spatial gradient). Detailed derivation can be found in Scovazzi and Hughes [2007] or Donea et al. [2004]. We can denote the relative velocity between the material and the mesh as the convective velocity $\boldsymbol{c}$

$$\boldsymbol{c} = \boldsymbol{v} - \hat{\boldsymbol{v}}. \tag{3.11}$$

Since material time derivative is present only in the energy balance equation, we will rewrite it

$$\rho_i c_p \frac{\partial T}{\partial t} = \nabla \cdot (k \nabla T) - \rho_i c_p (\boldsymbol{c} \cdot \nabla T). \tag{3.12}$$

3.2 Cartesian geometry

In order to solve the sets of equations and boundary conditions given in Sections 3.1.1 and 3.1.2 by finite element method (FEM), we have to transform them into a weak form [Logg et al., 2012, Alnæs et al., 2015].

In this section, the weak form will be derived in Cartesian coordinates. This will be useful for locally scaled problems and geometries where curvature of the shell can be neglected (i.e. if $(R_i/R_o)^2 \approx 1$, where R_i and R_o are the inner and the outer radii of the shell, respectively).

3.2.1 Governing equations and boundary conditions

Mass balance

We multiply the Equation (3.1) by a scalar test function ν and integrate over the domain Ω

$$0 = \int_\Omega (\nabla \cdot \boldsymbol{v})\nu \ \ \mathrm{d}x. \tag{3.13}$$

Momentum balance

We multiply Equation (3.2) by a vector test function $\boldsymbol{\mu}$ and integrate over the domain Ω. By applying Green's first identity on the viscous term

$$\begin{aligned}\int_\Omega [\nabla \cdot \eta(\nabla \boldsymbol{v} + \nabla^T \boldsymbol{v})] \cdot \boldsymbol{\mu} \ \mathrm{d}x = &\int_\Gamma \boldsymbol{n} \cdot \eta(\nabla \boldsymbol{v} + \nabla^T \boldsymbol{v}) \cdot \boldsymbol{\mu} \ \mathrm{d}S \\ &- \int_\Omega \eta(\nabla \boldsymbol{v} + \nabla^T \boldsymbol{v}) : \nabla^T \boldsymbol{\mu} \ \mathrm{d}x,\end{aligned} \tag{3.14}$$

and on the pressure term

$$-\int_\Omega \nabla p \cdot \boldsymbol{\mu} \ \mathrm{d}x = -\int_\Gamma p(\boldsymbol{\mu} \cdot \boldsymbol{n}) \ \mathrm{d}S + \int_\Omega p(\nabla \cdot \boldsymbol{\mu}) \ \mathrm{d}x, \tag{3.15}$$

we get two surface integrals which will be zero for all boundary conditions (3.6, 3.8 and 3.9). In case of the free-slip boundary condition, it is provided by

$$\begin{aligned}\boldsymbol{\mu} \cdot \boldsymbol{n} &= 0, \\ (\boldsymbol{\sigma} \cdot \boldsymbol{n})_t &= 0.\end{aligned} \tag{3.16}$$

Expanding the boundary integral of (3.14) as

$$\int_\Gamma [(\boldsymbol{n} \cdot \boldsymbol{\sigma})_n \boldsymbol{n} + (\boldsymbol{n} \cdot \boldsymbol{\sigma})_t \boldsymbol{t}] \cdot (\boldsymbol{\mu}_n \boldsymbol{n} + \boldsymbol{\mu}_t \boldsymbol{t}) \ \mathrm{d}S,$$

the normal component will be equal to zero due to the former condition in (3.16), the tangent component (and boundary integral in (3.15)) due to the latter condition. In case of the no slip condition, both boundary integrals in (3.14) and (3.15) are individually equal to zero due to

$$\boldsymbol{\mu} = \boldsymbol{0},$$

and in case of the free surface condition, their sum is equal to zero due to

$$[-p\boldsymbol{I} + \eta(\nabla \boldsymbol{v} + \nabla^T \boldsymbol{v})] \cdot \boldsymbol{n} = \boldsymbol{0}.$$

Then it holds

$$0 = \int_\Omega p(\nabla \cdot \boldsymbol{\mu}) - \rho_i(1 - \alpha(T - T_{\mathrm{ref}}))g(\boldsymbol{e_z} \cdot \boldsymbol{\mu}) - \eta(\nabla \boldsymbol{v} + \nabla^T \boldsymbol{v}) : \nabla^T \boldsymbol{\mu} \ \ \mathrm{d}x, \tag{3.17}$$

where we replaced $\boldsymbol{g}$ by $-g\boldsymbol{e_z}$.

In the case of free surface it is necessary to implement a stabilisation term, which prevents the free surface from oscillations due to diverging velocity [Kaus et al., 2010]. Although a sufficiently small timestep could ensure that as well, the

stabilisation term works well with CFL timestep criterion (discussed later). For the top free surface the term is:

$$-\int_{\Gamma_{\text{top}}} \lambda g \Delta t \rho_{\text{i}}[1-\alpha(T_{\text{top}}-T_{\text{ref}})](\boldsymbol{v}\cdot\boldsymbol{n})(\boldsymbol{\mu}\cdot\boldsymbol{e_z})\ \mathrm{d}S, \tag{3.18}$$

and for the bottom free surface

$$+\int_{\Gamma_{\text{bottom}}} \lambda g \Delta t\{\rho_{\text{w}}-\rho_{\text{i}}[1-\alpha(T_{\text{bot}}-T_{\text{ref}})]\}(\boldsymbol{v}\cdot\boldsymbol{n})(\boldsymbol{\mu}\cdot\boldsymbol{e_z})\ \mathrm{d}S, \tag{3.19}$$

with λ a constant, Δt a timestep and ρ_{w} is the ocean density beneath the ice shell.

If the free surface is an ice/ocean interface, there is a force due to density contrast acting on the boundary. This force is prescribed in the following form

$$+\int_{\Gamma_{\text{bottom}}} g(z\rho_{\text{w}}-H\rho_{\text{i}})(\boldsymbol{n}\cdot\boldsymbol{\mu})\ \mathrm{d}S, \tag{3.20}$$

where z is the vertical coordinate of the bottom surface and H is thickness of the shell. The term $-gH\rho_{\text{i}}$ represents a hydrostatic pressure that acts in the boundary. The term $gz\rho_{\text{w}}$ enhances or reduces the hydrostatic pressure reflecting the topography of the bottom boundary. Figure 3.2 shows the ice/ocean interface in detail.

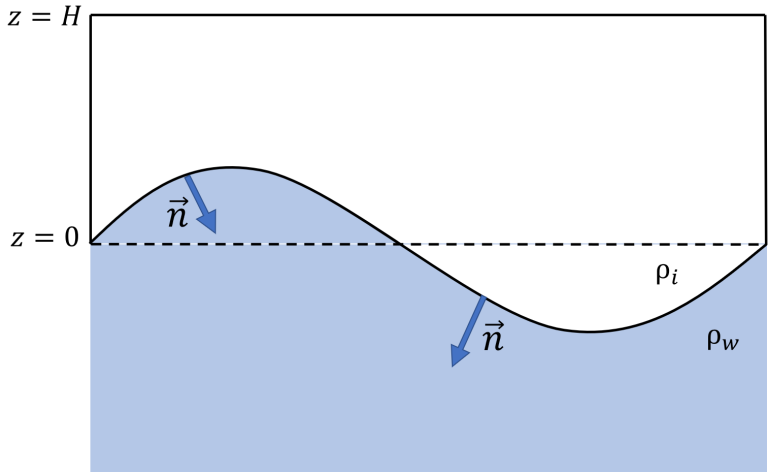

Figure 3.2: Detail of the ice/ocean interface.

Energy balance

We multiply Equation (3.12) by a scalar test function ϑ and integrate over the domain Ω. By applying Green's first identity to the conductive term we get

$$\int_\Omega \nabla\cdot(k\nabla T)\vartheta\ \mathrm{d}x = \int_\Gamma k\vartheta(\nabla T\cdot\boldsymbol{n})\ \mathrm{d}S - \int_\Omega k\nabla T\cdot\nabla\vartheta\ \mathrm{d}x.$$

The surface integral is equal to zero along the vertical boundaries because of Neumann boundary condition and along horizontal boundaries because of Dirichlet boundary condition ($\vartheta = 0$).

Then we can write the energy balance as

$$0 = \int_\Omega \rho_{\text{i}} c_p \frac{\partial T}{\partial t}\vartheta + k(\nabla T\cdot\nabla\vartheta) + \rho_{\text{i}} c_p(\boldsymbol{c}\cdot\nabla T)\vartheta\ \ \mathrm{d}x. \tag{3.21}$$

Free surface

Let Γ_{free} denote a free horizontal boundary and Γ_{fix} the fixed one. In Cartesian case, Equation (3.4) takes a form

$$\frac{\partial h}{\partial t} + \frac{\partial h}{\partial x} v_x = v_z. \tag{3.22}$$

Since it would be complicated to solve Equation (3.22) on the boundary, we prefer to solve the Laplace equation in the domain and prescribe Equation (3.22) as a boundary condition. We will demand the function h to be constant in z-direction, thus only z-component of the Laplace equation will be solved. The complete problem is described using the following equations:

$$\begin{aligned} \frac{\partial^2 h}{\partial z^2} &= 0 \quad \text{in } \Omega, \\ \frac{\partial h}{\partial t} + \frac{\partial h}{\partial x} v_x &= v_z \quad \text{at } \Gamma_{\text{free}}, \\ \frac{\partial h}{\partial z} &= 0 \quad \text{at } \Gamma_{\text{fix}}, \\ \frac{\partial h}{\partial x} &= 0 \quad \text{at } \Gamma_{\text{side}}. \end{aligned} \tag{3.23}$$

Because there is a derivative of h inthe boundary condition at Γ_{free} it is not possible to prescribe the boundary condition in a standard way. For this kind of conditions the Nitsche method is used [Juntunen and Stenberg, 2009]. Complete derivation of weak formulation can be found in Kihoulou [2019]. The weak form of problem (3.23) is then

$$\begin{aligned} 0 = &\int_\Omega \frac{\partial h}{\partial z}\frac{\partial \phi}{\partial z} \, \mathrm{d}x - \int_{\Gamma_{\text{free}}} \frac{\partial h}{\partial z}\phi \;\; \mathrm{d}S \\ &- \int_{\Gamma_{\text{free}}} \left[(h - h_k) + \Delta t \left(\frac{\partial h}{\partial x} v_x - v_z \right) \right] \left(\frac{\partial \phi}{\partial z} - \frac{\phi}{\gamma h_E} \right) \, \mathrm{d}S. \end{aligned} \tag{3.24}$$

where h denotes an elevation of a surface, h_k denotes its value in the previous timestep, Δt is a length of a timestep (see Equation 3.29), ϕ is a test function, $\gamma > 0$ is a stabilisation parameter and h_E is the element size on a free boundary. After solving this equation, the new boundary elevation is known and we can move the mesh by a mesh displacement vector $\boldsymbol{dh}$ defined as

$$\boldsymbol{dh}(x, z) = \frac{z}{H}(0, h - h_k) \tag{3.25}$$

for top free surface and

$$\boldsymbol{dh}(x, z) = \left(1 - \frac{z}{H}\right)(0, h - h_k) \tag{3.26}$$

for bottom free surface. The prefactor z/H and $(1 - z/H)$ for the top and the bottom free surface, respectively, distributes the mesh displacement in z-direction so that the free boundary moves with the maximum displacement given by Equation (3.24), while the opposite boundary is fixed.

The mesh velocity is then computed as

$$\boldsymbol{w} = \left(0, \frac{h - h_k}{\Delta t}\right) \tag{3.27}$$

and enters the energy balance through the convective velocity defined by (3.11).

3.2.2 Implementation (FEniCS, COMSOL 3.5a)

We have developed a computational program using a freely available software FEniCS designed for solving PDEs by finite element method (FEM)[Logg et al., 2012, Alnæs et al., 2015]. The FEniCS program was tested against another FEM software COMSOL 3.5a [Multiphysics, 1998], which is partly automatized. It is only necessary to choose geometry and material parameters. However, the geometry and material parameters have to be sufficiently simple.

FEniCS implementation

Element types

Because of stability, the most widely used elements for Stokes equations are the Taylor-Hood elements [Taylor and Hood, 1973], which consist of a continuous Lagrange element of order $q \geq 2$ ($q = 2$ in our case) for velocity and the same type but one order lower for pressure (see Figure 3.3). For temperature we use quadratic elements, while for mesh displacement linear elements. The classical Galerkin finite element method is used [Quarteroni and Valli, 1994].

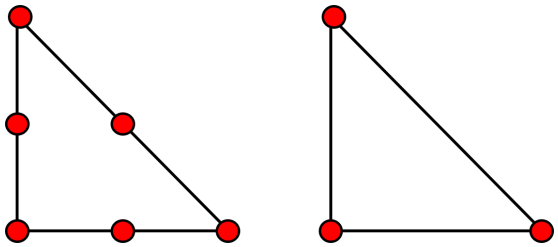

Figure 3.3: P_2 element for velocity and temperature (left), P_1 element for pressure and boundary elevation (right). Red dots represent computational nodes.

Time discretization

Since there are time derivatives in the energy balance and in the free surface equation, it is necessary to discretize them.

For energy balance we use Crank-Nicolson method

$$\frac{\partial T}{\partial t} = f(T)$$

$$\frac{T - T^k}{\Delta t} = \frac{1}{2}[f(T) + f^k(T)], \tag{3.28}$$

where index k denotes previous timestep. For the free surface equation we use implicit (backward) Euler method

$$\frac{\partial h}{\partial t} = f(h, v_x, v_z)$$

$$\frac{h - h_k}{\Delta t} = f(h, v_x, v_z). \tag{3.29}$$

The timestep is chosen to be the smaller one from the conductive and convective timestep

$$\Delta t = \min\{\Delta t_{\text{cond}}, \Delta t_{\text{conv}}\}$$

where Δt_{cond} and Δt_{conv} are given by the CFL criterion

$$\begin{aligned} \Delta t_{\text{conv}} &= c_{\text{CFL}} \cdot \frac{x_{\min}}{v_{\max}}, \\ \Delta t_{\text{cond}} &= c_{\text{CFL}} \cdot \frac{x_{\min}^2 \rho_{\text{i}} c_p}{k_{\max}}, \end{aligned} \tag{3.30}$$

where $x_{\min}$ is the size of the smallest mesh element, $v_{\max}$ is the maximum velocity in the domain and $k_{\max}$ is the maximum value of thermal conductivity and $c_{\text{CFL}} < 1$ is a positive constant, usually $c_{\text{CFL}} = 0.5$.

If the maximum temperature difference $\Delta T_{\max}$ before and after solving energy balance exceeds a threshold value ΔT_{thres}, we solve the energy balance again with a new, smaller timestep Δt_{new} given by

$$\Delta t_{\text{new}} = 0.9 \frac{\Delta T_{\text{thres}}}{\Delta T_{\max}} \Delta t_k, \tag{3.31}$$

where Δt_k is the previous timestep. This iteration reduces $\Delta T_{\max}$ approximately to the value of ΔT_{thres}.

COMSOL 3.5a implementation

COMSOL is mostly automatized software. User then has only to choose geometry, material parameters, which makes the problem implementation easy and straightforward.

Scheme in Figure 3.4 shows the structure of COMSOL 3.5a implementation. It consists of `Incompressible Navier-Stokes, Convection and conduction` and `Moving mesh` modules.

Element types

Taylor-Hood elements for Stokes problem are the default choice in Comsol, so are P_2 elements for energy balance. However, for moving mesh, P_2 elements are used, instead of P_1 which were used in FEniCS implementation.

Hierarchy of modules

If we solve thermo-mechanical problem, `Convection and conduction` has to be the rulling application module, since it solves evolution of temperature in time (the choice `Analysis type: Transient`). However, if we solve only mechanical

problem, rulling application mode is then `Moving mesh` module (again `Analysis type: Transient`).

Module `Moving mesh` also defines the reference frame which must be used by all other modules (`Defines frame: ALE`). Unfortunately, user cannot see the strong form of the equation which moves the mesh. We set `Mesh displacement: Free`, zero velocity at the fixed surface and prescribe velocity computed by `Navier-Stokes` module at the free surface. Time discretization and time stepping is fully governed by the software.

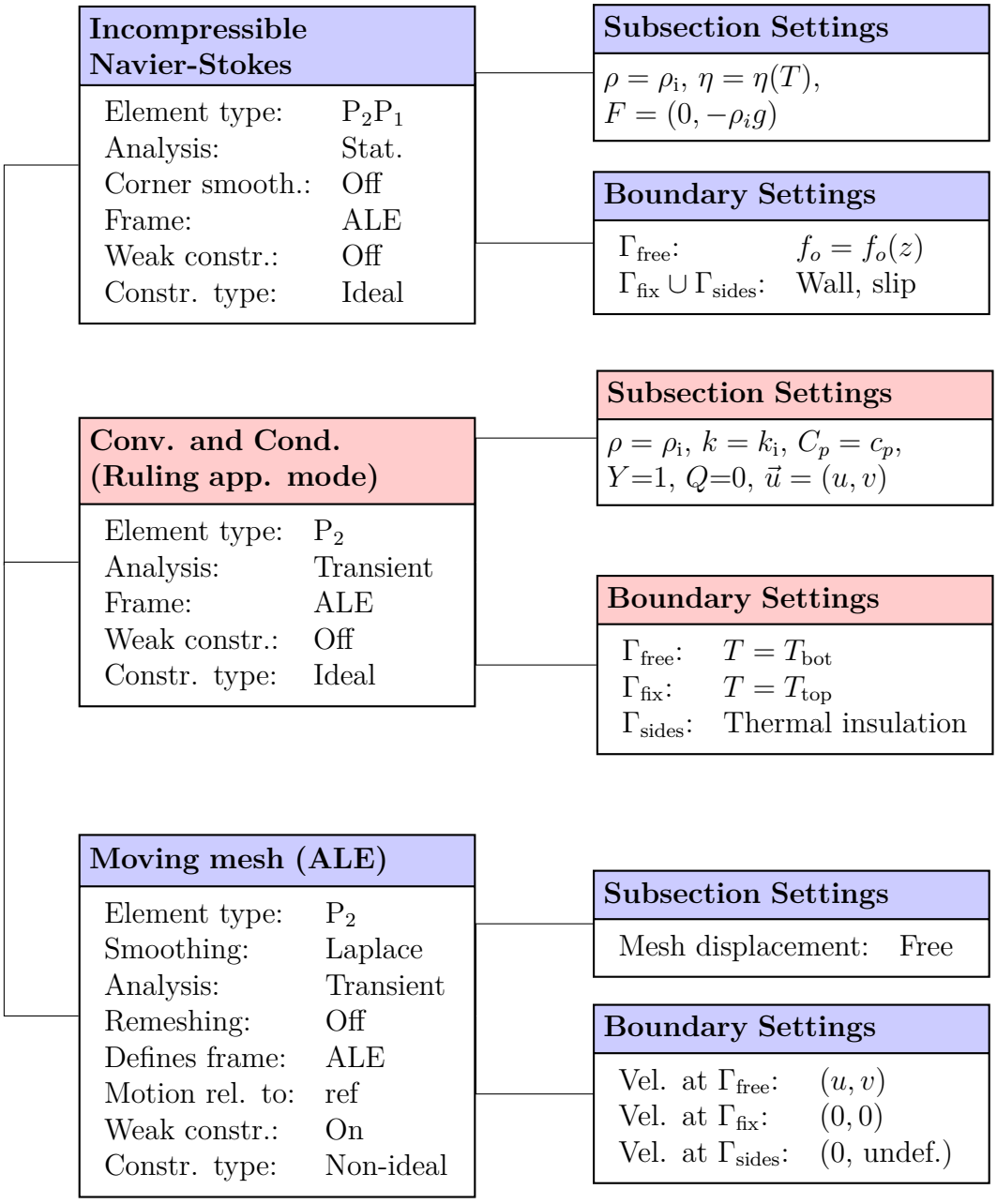

Figure 3.4: COMSOL 3.5a implementation diagram.

3.2.3 Numerical tests

The implementation of relaxation-advection problem was tested against a FEM software COMSOL 3.5a [Multiphysics, 1998].

Relaxation-advection with $\eta = const.$

The initial shape of the domain is a square with side of length H and a subtracted circle of radius $R = 5L/6$ (see Figure 3.5), so that the boundary (bottom case) is prescribed by

$$g(x) = (\sqrt{L^2 - 3x^2} - L/2)/\sqrt{3}$$

In order to satisfy boundary conditions, temperature profile has to be adapted to curved boundary. We used following relation

$$T(x,z) = T_{\text{bot}} + (T_{\text{top}} - T_{\text{bot}})\frac{z - g(x)}{L - g(x)}, \tag{3.32}$$

where $g(x)$ is bottom boundary shape. In case of top boundary, $g(x)$ and $T(x,z)$ are analogical.

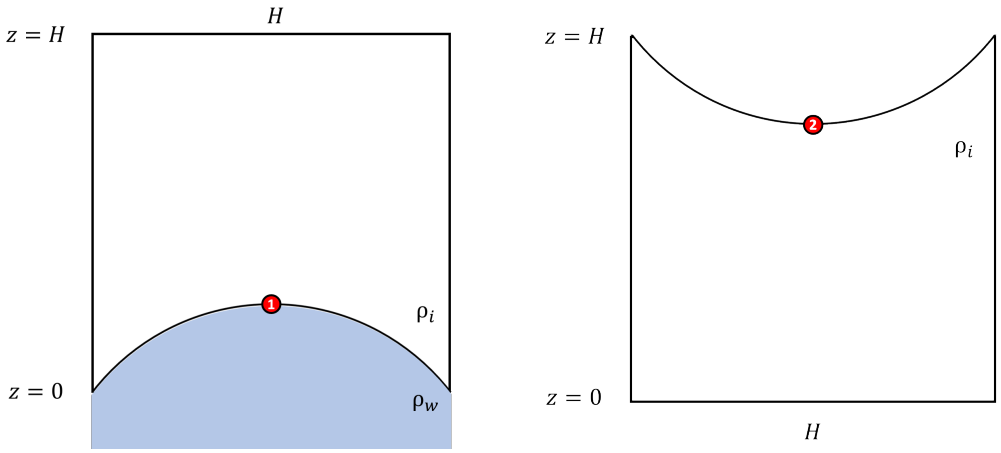

Figure 3.5: Geometry of test problem. Bottom free surface (left), top free surface (right). Tracked points are represented by red circle.

Table 3.1 summarizes parameters used for isoviscous test. Free slip boundary condition was applied everywhere but top/bottom boundary.

The relaxation part of the problem was tested by comparing the z-coordinate in the middle of a relaxing boundary with respect to time. Advection of the temperature field was tested by comparing the temperature along five straight lines with z coordinate given by

$$z_n = 50 + n \cdot 25 \text{ km}, \quad \text{n} \in [0, 4] \tag{3.33}$$

and at 11 different times given by

$$t_k = 3k \cdot 10^{11} \text{ s}, \quad \text{k} \in [0, 10]. \tag{3.34}$$

Height	H	150	km
Radius	R	125	km
Viscosity	η	10^{18}	$\mathrm{Pa} \cdot \mathrm{s}$
Ice density	ρ_{i}	920	$\mathrm{kg} \cdot \mathrm{m}^{-3}$
Water density	ρ_{w}	1000	$\mathrm{kg} \cdot \mathrm{m}^{-3}$
Gravity	g	0.617	$\mathrm{m} \cdot \mathrm{s}^{-2}$
Top temperature	T_{top}	50	K
Bottom temperature	T_{bot}	273	K
Conductivity	k_{i}	2.3	$\mathrm{W} \cdot \mathrm{m}^{-1} \cdot \mathrm{K}^{-1}$
Heat capacity	c_p	2100	$\mathrm{J} \cdot \mathrm{kg}^{-1} \cdot \mathrm{K}^{-1}$

Table 3.1: Test parameters.

Results

FEniCS code was tested both with and without the stabilisation term (Equations 3.19 and 3.18). Figure 3.6 shows the result of the relaxation part, Figure 3.7 shows the comparison for all five lines and chosen given by Equations (3.33) and (3.34). We observe that curves agree very well for both cases.

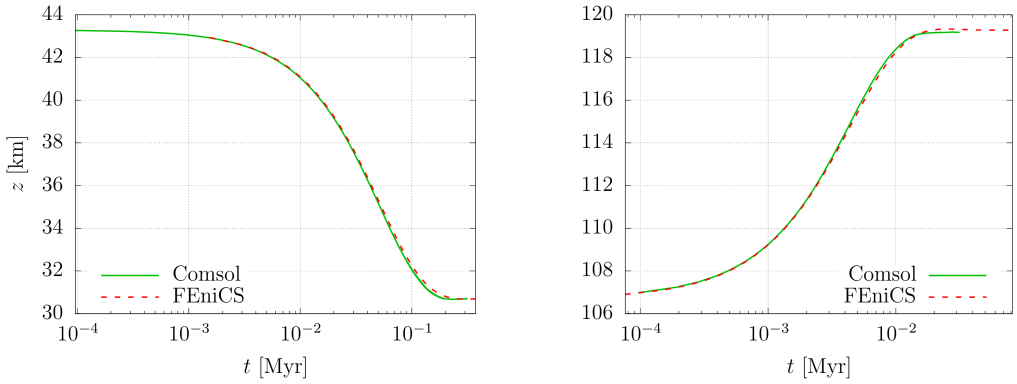

Figure 3.6: Relaxation curves for isoviscous case for bottom boundary, point 1 (left) and top boundary, point 2 (right).

Figure 3.7 shows the results of advective part. Temperature field is compared along the lines represented by (3.33). With increasing time (resp. k, times of screenshots are given by (3.34)) we observe, that curves get flatter, which is in agreement with expectation how the bottom boundary relaxes. Both FEniCS and Comsol results agree very well.

Relaxation-advection with $\eta = \eta(T)$

The relaxation part (for bottom boundary only) was also tested for temperature-dependent viscosity.

Because of non-uniform viscosity, we found more convenient to use smoothed boundary. As the bottom boundary, we used following Gaussian curve

$$g(x) = a \cdot \exp\left[-\frac{(x-b)^2}{2(c/6)^2}\right], \tag{3.35}$$

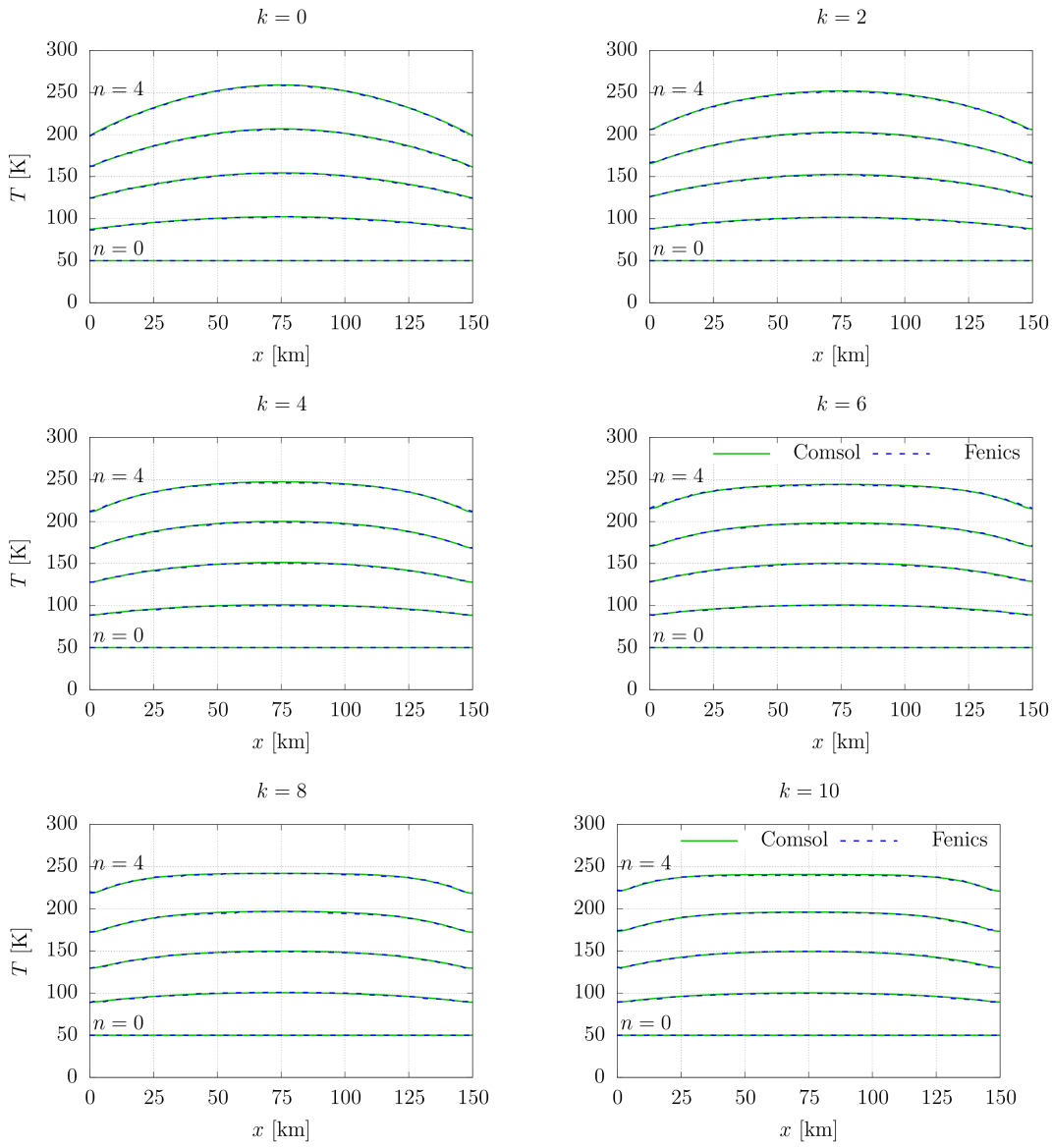

Figure 3.7: Advection part of the isoviscous test.

where $a = 30$ km, $b = 0$ km and $c = 150$ km. Hence the temperature was given by

$$T(x, z) = T_{\text{bot}} + (T_{\text{top}} - T_{\text{bot}}) \frac{z - g(x)}{L - g(x)}. \tag{3.36}$$

For viscosity we use the following formula [Tobie et al., 2005]

$$\eta(T) = \eta_0 \cdot \exp\left[\frac{Q}{R} \cdot \left(\frac{1}{T} - \frac{1}{T_m}\right)\right], \tag{3.37}$$

where η_0 is a viscosity at melting temperature T_m, Q is an activation energy and R is the molar gas constant. Since COMSOL was able to solve relaxation with maximum viscosity contrast of 3 orders, we chose sufficiently small Q that satisfies this condition. Parameter values are listed in Table 3.2.

Figure 3.8 summarizes the initial temperature and viscosity field and the smoothed geometry. In Figure 3.9, relaxation curves for Points 1 and 2 are

compared for FEniCS and Comsol calculations. Results of the test agree very well.

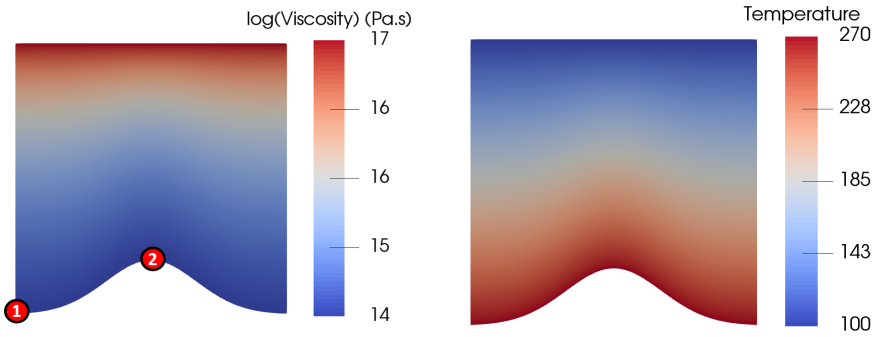

Figure 3.8: The initial viscosity (left) and temperature (right) fields with Points 1 and 2 for relaxation curve.

Height	H	150	km
Ice density	ρ_{i}	920	$\mathrm{kg} \cdot \mathrm{m}^{-3}$
Water density	ρ_{w}	1000	$\mathrm{kg} \cdot \mathrm{m}^{-3}$
Gravity	g	0.617	$\mathrm{m} \cdot \mathrm{s}^{-2}$
Top temperature	T_{top}	100	K
Bottom temperature	T_{bot}	270	K
Reference viscosity	η_0	10^{14}	$\mathrm{Pa} \cdot \mathrm{s}$
Activation energy	Q	10^4	J
Conductivity	k_{i}	2.3	$\mathrm{W} \cdot \mathrm{m}^{-1} \cdot \mathrm{K}^{-1}$
Heat capacity	c_p	2100	$\mathrm{J} \cdot \mathrm{kg}^{-1} \cdot \mathrm{K}^{-1}$

Table 3.2: Test parameters for temperature-dependent viscosity.

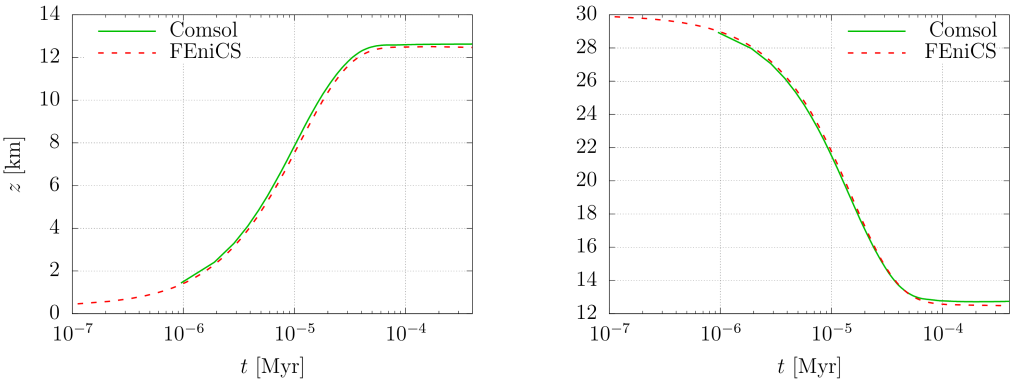

Figure 3.9: Relaxation curves for temperature dependent viscosity for bottom boundary, point 1 (left) and point 2 (right).

3.3 Cylindric geometry

When we are interested in processes whose dimensions are comparable to or larger than the shell thickness, its curvature starts to affect the problem. Since we will

be interested in relaxation of a ∼1000 km crater on a 100 – 200 km thick shell, it is necessary to take the curvature into consideration. Since three-dimensional problem would be extremely computationally expensive, we will solve it as two-dimensional axisymmetric problem, which is, regarding crater morphology, reasonable.

Since FEniCS software operates only in Cartesian coordinate system, we will reformulate differential operators in cylindrical coordinates. In this section, we derive the form of differential operators in cylindrical coordinates.

3.3.1 ∇ and $\nabla\cdot$ in cylindrical coordinates

We define cylindrical coordinates (r, φ, z) in a following way

$$\begin{aligned} x &= r\cos\varphi, \\ y &= r\sin\varphi, \\ z &= z, \end{aligned} \tag{3.38}$$

where r is distance from symmetry axis, φ is longitude and z is vertical coordinate with the same meaning as the Cartesian one (see Figure 3.10).

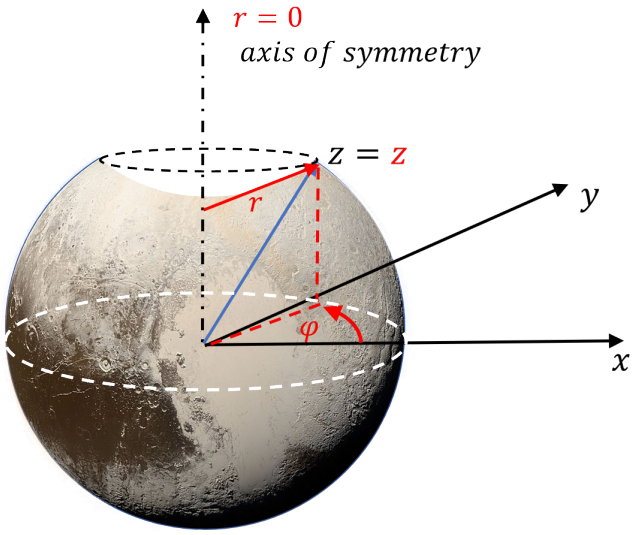

Figure 3.10: Cartesian (black) and cylindrical (red) coordinate system.

For transition between Cartesian and generally curvilinear coordinates, it is necessary to introduce Lamé parameters [Martinec, 2011]

$$h_i = \sqrt{\sum_k \left(\frac{\partial y_k}{\partial x_i}\right)^2}, \tag{3.39}$$

where y_k denotes Cartesian coordinate and x_i curvilinear coordinate. Uniqueness of this map is conditioned by non-zero Jacobian and differentiability of x_k. For cylindric coordinates we get

$$\begin{aligned} h_r &= 1, \\ h_\varphi &= r, \\ h_z &= 1. \end{aligned} \tag{3.40}$$

Inverse Jacobian of this transformation is given by

$$J^{-1} = \left|\frac{\partial x_k}{\partial y_l}\right| = \begin{vmatrix} \cos\varphi & r\sin\varphi & 0 \\ -r\sin\varphi & r\cos\varphi & 0 \\ 0 & 0 & 1 \end{vmatrix} = r \tag{3.41}$$

We will need formulas for gradient of a scalar, divergence of a vector and gradient of a vector. The generalized formulas are (following Martinec [2011]):

$$\nabla s = \sum_k \frac{\vec{e_k}}{h_k}\frac{\partial s}{\partial x_k}, \tag{3.42}$$

$$\nabla \cdot \boldsymbol{v} = \frac{1}{h_1 h_2 h_3}\left[\frac{\partial}{\partial x_1}(h_2 h_3 v_1) + \frac{\partial}{\partial x_2}(h_1 h_3 v_2) + \frac{\partial}{\partial x_3}(h_1 h_2 v_3)\right], \tag{3.43}$$

$$(\nabla \boldsymbol{v})_{lk} = \begin{cases} \dfrac{1}{h_k}\left(\dfrac{\partial v_k}{\partial x_k} + \sum\limits_{m,m\neq k}\dfrac{1}{h_m}\dfrac{\partial h_k}{\partial x_m}v_m\right) & \text{for } l = k \\ \dfrac{1}{h_k}\left(\dfrac{\partial v_l}{\partial x_k} - \dfrac{1}{h_l}\dfrac{\partial h_k}{\partial x_l}v_k\right) & \text{for } l \neq k. \end{cases} \tag{3.44}$$

In the following text, rows are denoted by an index k, columns by an index l.

Gradient of a scalar

Substituting (3.40) into (3.42) we get

$$\begin{aligned} \nabla s &= \boldsymbol{e_r}\frac{\partial s}{\partial r} + \frac{\boldsymbol{e_\varphi}}{r}\frac{\partial s}{\partial \varphi} + \boldsymbol{e_z}\frac{\partial s}{\partial z} \\ &\overset{s=s(r,z)}{=} \boldsymbol{e_r}\frac{\partial s}{\partial r} + \boldsymbol{e_z}\frac{\partial s}{\partial z}. \end{aligned} \tag{3.45}$$

In the last step we used the assumption of axisymmetry (functions are constant in longitude φ), meaning that any derivative with respect to φ is equal to zero. Used further, it will be always denoted by $\overset{\cdot\,=\,\cdot(r,z)}{=}$ sign with the name of the axisymmetric quantity. We observe that a gradient of a scalar in cylindrical coordinates stays the same as in Cartesian coordinates.

Divergence of a vector

Substituting (3.40) into (3.43) we get

$$\begin{aligned} \nabla \cdot \boldsymbol{v} &= \frac{1}{r}\left[\frac{\partial}{\partial r}(r v_r) + \frac{\partial}{\partial \varphi}(v_\varphi) + \frac{\partial}{\partial z}(r v_z)\right] \\ &= \frac{\partial v_r}{\partial r} + \frac{v_r}{r} + \frac{1}{r}\frac{\partial v_\varphi}{\partial \varphi} + \frac{\partial v_z}{\partial z} \\ &\overset{\boldsymbol{v}=\boldsymbol{v}(r,z)}{=} \frac{\partial v_r}{\partial r} + \frac{v_r}{r} + \frac{\partial v_z}{\partial z}. \end{aligned} \tag{3.46}$$

Compared to Cartesian divergence, there is an extra term v_r/r.

Gradient of a vector

For cylindrical coordinates, the derivatives $\frac{\partial h_k}{\partial x_l}$ in 3.44 are equal to zero for all combinations of l and k but $l, k = 1, 2$ and $2, 2$, where it is equal to 1 (because the only nonzero Lamé parameter derivative is that of $h_\varphi = r$). Substituting (3.40) into (3.44) we get

$$(\nabla \boldsymbol{v})_{12} = \frac{1}{r}\left(\frac{\partial v_r}{\partial \varphi} - \frac{1}{1}\frac{\partial r}{\partial r} v_\varphi\right) = \frac{1}{r}\left(\frac{\partial v_\varphi}{\partial \varphi} + v_\varphi\right)$$

$$(\nabla \boldsymbol{v})_{22} = \frac{1}{r}\left(\frac{\partial v_\varphi}{\partial \varphi} + \frac{1}{1}\frac{\partial r}{\partial r} v_r\right) = \frac{1}{r}\left(\frac{\partial v_\varphi}{\partial \varphi} + v_r\right)$$

$$\nabla \boldsymbol{v} = \begin{pmatrix} \frac{\partial v_r}{\partial r} & \frac{1}{r}\frac{\partial v_r}{\partial \varphi} - \frac{v_\varphi}{r} & \frac{\partial v_r}{\partial z} \\ \frac{\partial v_\varphi}{\partial r} & \frac{1}{r}\frac{\partial v_\varphi}{\partial \varphi} + \frac{v_r}{r} & \frac{\partial v_\varphi}{\partial z} \\ \frac{\partial v_z}{\partial r} & \frac{1}{r}\frac{\partial v_z}{\partial \varphi} & \frac{\partial v_z}{\partial z} \end{pmatrix} \overset{\boldsymbol{v}=\boldsymbol{v}(r,z)}{=} \begin{pmatrix} \frac{\partial v_r}{\partial r} & 0 & \frac{\partial v_r}{\partial z} \\ 0 & \frac{v_r}{r} & 0 \\ \frac{\partial v_z}{\partial r} & 0 & \frac{\partial v_z}{\partial z} \end{pmatrix} \tag{3.47}$$

We can thus write (in terms of velocity $\boldsymbol{v}$ and its test function $\boldsymbol{\mu}$ used later)

$$(\nabla \boldsymbol{v} + \nabla^{\mathrm{T}} \boldsymbol{v}) : \nabla^{\mathrm{T}} \boldsymbol{\mu} = \begin{pmatrix} 2\frac{\partial v_r}{\partial r} & 0 & \frac{\partial v_r}{\partial z} + \frac{\partial v_z}{\partial r} \\ 0 & 2\frac{v_r}{r} & 0 \\ \frac{\partial v_z}{\partial r} + \frac{\partial v_r}{\partial z} & 0 & 2\frac{\partial v_z}{\partial z} \end{pmatrix} : \begin{pmatrix} \frac{\partial \mu_r}{\partial r} & 0 & \frac{\partial \mu_z}{\partial r} \\ 0 & \frac{\mu_r}{r} & 0 \\ \frac{\partial \mu_r}{\partial z} & 0 & \frac{\partial \mu_z}{\partial z} \end{pmatrix}$$

$$= \begin{pmatrix} 2\frac{\partial v_r}{\partial r} & \frac{\partial v_r}{\partial z} + \frac{\partial v_z}{\partial r} \\ \frac{\partial v_z}{\partial r} + \frac{\partial v_r}{\partial z} & 2\frac{\partial v_z}{\partial z} \end{pmatrix} : \begin{pmatrix} \frac{\partial \mu_r}{\partial r} & \frac{\partial \mu_z}{\partial r} \\ \frac{\partial \mu_r}{\partial z} & \frac{\partial \mu_z}{\partial z} \end{pmatrix} + 2\frac{v_r}{r}\frac{\mu_r}{r} \tag{3.48}$$

There is a part identical to Cartesian case and an extra term $2\frac{v_r}{r}\frac{\mu_r}{r}$.

3.3.2 Spherical geometry

Equations were chosen to be expressed in cylindrical coordinates because we needed to identify axes x and z (which form a right angle) with axes r and z.

Even though the coordinate system is cylindrical, the geometry of the problem will be spherical (see Figure 3.11). It is thus advantageous to define scalar radius R, radial unit vector $\boldsymbol{R} = \boldsymbol{R}(r, z)$ and its tangent unit vector $\boldsymbol{T} = \boldsymbol{T}(r, z)$

$$\begin{aligned} R &= \sqrt{r^2 + z^2}, \\ \boldsymbol{R} &= \left(\frac{r}{\sqrt{r^2 + z^2}}, \frac{z}{\sqrt{r^2 + z^2}}\right), \\ \boldsymbol{T} &= (-R_z, R_r). \end{aligned} \tag{3.49}$$

We will use them later to describe the direction of gravity and they will appear in momentum balance and free surface equation.

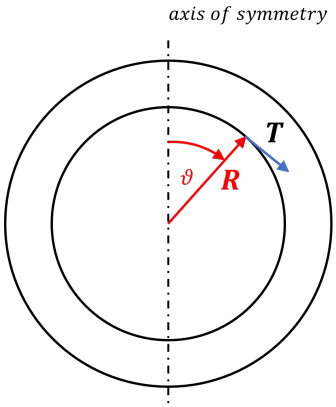

Figure 3.11: Auxilliary spherical coordinates. Lattitude ϑ, radial unit vector $\boldsymbol{R}$ and tangent unit vector $\boldsymbol{T}$.

3.3.3 Governing equations and boundary conditions

Writing the weak form we proceed similarly as in the Cartesian case. However, we will employ one simplification which will be demonstrated on the mass balance.

Mass balance

Denoting (3.46) as $\nabla_{\text{cyl}}\cdot$ (cylindric divergence), we can write the equation of continuity as

$$0 = \int_\Omega (\nabla_{\text{cyl}} \cdot \boldsymbol{v}) \nu r \, \mathrm{d}\Omega_{r\varphi z},$$

where ν is a scalar test function and r is a Jacobian resulting from coordinate transformation. Since our problem will be axisymmetric, none of the integrands will depend on φ coordinate. We can then integrate with respect to φ, which gives 2π

$$0 = 2\pi \int_\Omega (\nabla_{\text{cyl}} \cdot \boldsymbol{v}) \nu r \, \mathrm{d}\Omega_{rz}.$$

Since this term will result from every integral, we can divide the whole equation by 2π

$$0 = \int_\Omega (\nabla_{\text{cyl}} \cdot \boldsymbol{v}) \nu r \, \mathrm{d}\Omega_{rz}. \tag{3.50}$$

Momentum balance

Denoting $D(\boldsymbol{v})$ as a symmetric gradient of the velocity and $\nabla\boldsymbol{\mu}$ gradient of its test function

$$D(\boldsymbol{v}) = \frac{1}{2}\begin{pmatrix} 2\dfrac{\partial v_r}{\partial r} & \dfrac{\partial v_z}{\partial r} + \dfrac{\partial v_r}{\partial z} \\ \dfrac{\partial v_z}{\partial r} + \dfrac{\partial v_r}{\partial z} & 2\dfrac{\partial v_z}{\partial z} \end{pmatrix}, \quad \nabla\boldsymbol{\mu} = \begin{pmatrix} \dfrac{\partial \mu_r}{\partial r} & \dfrac{\partial \mu_z}{\partial r} \\ \dfrac{\partial \mu_r}{\partial z} & \dfrac{\partial \mu_z}{\partial z} \end{pmatrix},$$

we can write momentum equation as

$$0 = \int_\Omega \Big[p\nabla_{\text{cyl}} \cdot \boldsymbol{\mu} - \rho_i(1 - \alpha(T - T_{\text{ref}}))g(\boldsymbol{R} \cdot \boldsymbol{\mu}) \\ - 2\eta D(\boldsymbol{v}) : \nabla^T \boldsymbol{\mu} - 2\eta \frac{v_r \mu_r}{r^2} \Big] r \ \mathrm{d}\Omega_{rz}. \tag{3.51}$$

Again we, use the stabilization term for bottom free surface

$$+ \int_{\Gamma_{\text{free}}} [\lambda(\rho_{\text{w}} - \rho_{\text{i}}(1 - \alpha(T - T_{\text{ref}})))\Delta t(\boldsymbol{v} \cdot \boldsymbol{n})(\boldsymbol{R} \cdot \boldsymbol{\mu})]\, r \ \ \mathrm{d}S_{rz}$$

and for top free surface

$$- \int_{\Gamma_{\text{free}}} [\lambda\rho_{\text{i}}(1 - \alpha(T - T_{\text{ref}}))\Delta t(\boldsymbol{v} \cdot \boldsymbol{n})(\boldsymbol{R} \cdot \boldsymbol{\mu})]\, r \ \ \mathrm{d}S_{rz}.$$

In case of an ice/ocean interface, the force due to the density contrast acting on the bottom boundary will read

$$+ \int_{\Gamma_{\text{bottom}}} g[(R - R_i)\rho_{\text{w}} - (R_o - R_i)\rho_{\text{i}}](\boldsymbol{n} \cdot \boldsymbol{\mu}) r \ \mathrm{d}S_{rz}, \tag{3.52}$$

where R_i and R_o are inner and outer radius of the shell respectively.

Energy balance

Energy balance contains only a gradient of a scalar, which was shown to have the same form as in Cartesian coordinates. It thus reads

$$0 = \int_\Omega \left[\rho_{\text{i}} c_p \frac{\partial T}{\partial t}\vartheta + k(\nabla T \cdot \nabla \vartheta) + \rho_{\text{i}} c_p (\boldsymbol{c} \cdot \nabla T)\vartheta \right] r \ \mathrm{d}\Omega_{rz}. \tag{3.53}$$

Nitsche method for Stokes problem

In FEniCS software, it is possible to prescribe free slip only on a boundary parallel with coordinate axes by fixing one component of the velocity equal to zero. For the other boundaries (oblique or curved), normal component of the velocity is dependent on both x, y or r, z coordinates.

Nitsche method allows us to prescribe this condition on such boundaries [Juntunen and Stenberg, 2009]. Following Freund and Stenberg [1995], for Stokes problem we can write momentum equation as (3.51) with two additional terms to impose free slip condition weakly

$$+ \int_\Gamma [(-\nu \boldsymbol{I} + 2\eta D(\boldsymbol{\mu})) \cdot \boldsymbol{v}] \cdot \boldsymbol{n} \ \mathrm{d}S, \\ \pm \int_\Gamma [(-p\boldsymbol{I} + 2\eta D(\boldsymbol{v})) \cdot \boldsymbol{\mu}] \cdot \boldsymbol{n} \ \mathrm{d}S, \tag{3.54}$$

where the second term can be symmetric (+ sign) or antisymmetric (- sign), and a stabilisation term

$$-\frac{\eta\beta}{h_{\max}} \int_\Gamma (\boldsymbol{v} \cdot \boldsymbol{n})(\boldsymbol{\mu} \cdot \boldsymbol{n}) \ \mathrm{d}S,$$

where $\beta > 0$ is a parameter large enough and $h_{\max}$ maximum element size. We also have the liberty while choosing between symmetric and antisymmetric form of a term in (3.54), which weakly enforces the slip condition. However, we concluded that symmetric term gives better results.

Free surface

Since we are describing spherical surface, we will use spherical vectors introduced in Figure 3.11. In analogy to the Cartesian case we write

$$\begin{aligned} \frac{\partial^2 h}{\partial R^2} &= 0 \quad \text{in } \Omega, \\ \frac{\partial h}{\partial t} + \frac{\partial h}{\partial T} v_T &= v_R \quad \text{at } \Gamma_{\text{free}}, \\ \frac{\partial h}{\partial R} &= 0 \quad \text{at } \Gamma_{\text{fix}}, \\ \frac{\partial h}{\partial T} &= 0 \quad \text{at } \Gamma_{\text{side}}, \end{aligned} \tag{3.55}$$

where v_R and v_T is radial and tangential velocity component, respectively.

Applying Nitsche method, we get the weak form

$$\begin{aligned} 0 = &\int_\Omega (\nabla h \cdot \boldsymbol{R})(\nabla \phi \cdot \boldsymbol{R}) \, \mathrm{d}x - \int_{\Gamma_{\text{free}}} \frac{\partial h}{\partial \boldsymbol{n}} \phi \, \mathrm{d}s \\ &- \int_{\Gamma_{\text{free}}} \left[(h - h_k) + \Delta t \left((\nabla h \cdot \boldsymbol{T})(\boldsymbol{v} \cdot \boldsymbol{T}) - \boldsymbol{v} \cdot \boldsymbol{n} \right) \right] \left(\frac{\partial \phi}{\partial \boldsymbol{n}} - \frac{\phi}{\gamma h_E} \right) \mathrm{d}s. \end{aligned} \tag{3.56}$$

In analogy to Cartesian geometry, we distribute the mesh displacement by

$$\boldsymbol{dh}(R, \vartheta) = \frac{R - R_{in}}{H} (h - h_k, 0)$$

in terms of spherical coordinates R, ϑ. However, we need to express the displacement in cylindrical coordinates r, z. We can achieve that by projecting unit radial vector in vertical and horizontal coordinate (see Equation 3.49). Then we can write

$$\boldsymbol{dh}(r, z) = \frac{\sqrt{r^2 + z^2} - R_{in}}{H} (h - h_k) \left(\frac{r}{\sqrt{r^2 + z^2}}, \frac{z}{\sqrt{r^2 + z^2}} \right) \tag{3.57}$$

for the top surface. For the bottom surface we use a prefactor $1 - \dfrac{\sqrt{r^2 + z^2} - R_{in}}{H}$.

3.3.4 Implementation (COMSOL 3.5a, FEniCS, FORTRAN90)

COMSOL 3.5a implementation

The implementation of a convection in axisymmetric spherical geometry is analogous to the scheme described in Figure 3.4. We only have to choose space dimension `Axial symmetry (2D)`. Since we only solve temperature evolution, we omit the `Moving mesh` module.

FORTRAN90 implementation

For solving relaxation by spectral method, we use program developed in author's bachelor thesis [Kihoulou, 2019].

FEniCS implementation

The ice shell has in many cases high aspect ratio (ratio of horizontal dimension to vertical one): If we consider uniform mesh dense enough with element aspect ratio 1:1, the problem becomes computationally expensive. Time consumption can be reduced in at least three ways: by the choice of element diagonal type, by non-uniform meshing (fine only where necessary) and by parallelization.

Element diagonal type

While creating a mesh in FEniCS, one can choose between right (default) diagonal, left diagonal and both of them (crossed), see Figure 3.12. Although mesh with only one diagonal contains less computational nodes and thus provides faster computation, it gave inaccurate results in our tests. When using crossed elements, this inaccuracy did not occur.

(a) P_1 element (b) P_2 element

Figure 3.12: A fragment of mesh composed of P_1 and P_2 elements respectively with choice `right` and `crossed` diagonal.

(Non)uniform mesh

When creating mesh it is also important to keep aspect ratio of elements as small as possible. In our test cases, we chose uniform mesh with 50 elements in radial and 361 in latitudinal direction. For 150 km thick shell this gives resolution 3×10 km, thus aspect ratio ≈ 3, which is still acceptable.

For relaxation of craters we created non-uniform mesh denser in the proximity of crater-shaped boundary and coarser in the rest of the domain. Refinement of the mesh is done directly in FEniCS code, so there is no need to create mesh externally. Figure 3.13 shows the example of such refinement. For the relaxation simulations both refinement and paralellization were necessary.

Program paralellization

Because of high number of computational nodes and thus large stiffness matrices to be solved and stored, we use MPI (Message Passing Interface) paralellization [Dalcín et al., 2005].

3.3.5 Numerical tests

The great advantage of COMSOL software is that it offers 2D axisymmetric geometry. Therefore formulation of this problem in COMSOL was equally straightforward as of the Cartesian one. Unfortunately, in 3.5a version we were not succesful to use `Moving mesh` module in axisymmetric setting. We thus divided the test

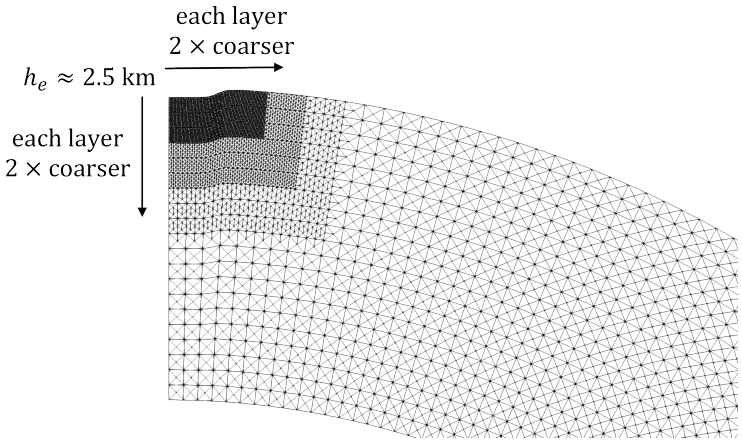

Figure 3.13: Mesh refinement example for crater of diameter of 100 km on a shell of outer radius 1188 km.

of axisymmetric spherical geometry into two parts: convective part (COMSOL 3.5a) and relaxation part (FORTRAN).

Convective test

The convective part of the problem was tested by comparing radial temperature profile and RMS velocity for a radially ascending temperature anomaly.

As a domain we chose only a segment of a shell and placed in the middle a positive Gaussian shaped temperature anomaly given by

$$\Delta T = 200 \cdot \exp\left[\frac{-(\vartheta - \vartheta_A)^2}{1}\right] \cdot \exp\left[-\frac{(R - R_A)^2}{5 \cdot 10^8}\right], \tag{3.58}$$

where ϑ and R are spherical latitude and radius, respectively, ϑ_A and R_A are latitude and radial distance of temperature anomaly, respectively, see Figure 3.14. The line where the temperature was compared is given by $\vartheta = \vartheta_A$. RMS velocity can be computed as

$$v_{\mathrm{RMS}} = \int_\Omega \sqrt{\boldsymbol{v} \cdot \boldsymbol{v}}\; r \;\; \mathrm{d}\Omega_{rz}. \tag{3.59}$$

As a boundary condition, we used fixed temperature ($\Delta T = 0$ K) and free slip everywhere. Parameters for convection test are summarized in Table 3.3.

Results

Figure 3.15 shows the ascending temperature anomaly (these are only fragments, the real geometry is shown in Figure 3.14). We can see outward radial motion which transforms to tangent at the boundary. The anomaly is getting flatter as it approches the boundary because of the free slip condition.

Radial temperature profile at $\vartheta = 24°$ is shown in Figure 3.16. Because of the steep temperature gradient near the boundary, there are oscillations in COMSOL profiles. Nevertheless, we observe that the result is satisfactory. The agreement for RMS velocity is perfect (Figure 3.17).

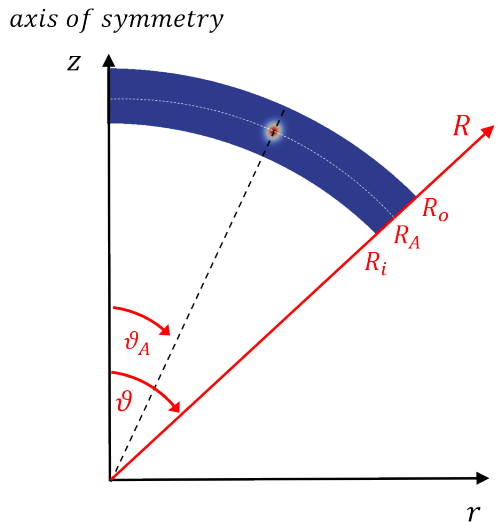

Figure 3.14: Geometry for the convection test.

Inner radius	R_i	1038	km
Outer radius	R_o	1188	km
Radial distance of anomaly	R_A	1113	km
Latitude of anomaly	ϑ_A	24	°
Ice density	ρ_i	920	$\mathrm{kg \cdot m^{-3}}$
Viscosity	η	10^{18}	$\mathrm{Pa \cdot s}$
Gravity	g	0.617	$\mathrm{m \cdot s^{-2}}$
Boundary ΔT	ΔT	0	K
Conductivity	k_i	2.3	$\mathrm{W \cdot m^{-1} \cdot K^{-1}}$
Heat capacity	c_p	2100	$\mathrm{J \cdot kg^{-1} \cdot K^{-1}}$

Table 3.3: Test parameters for the convection test.

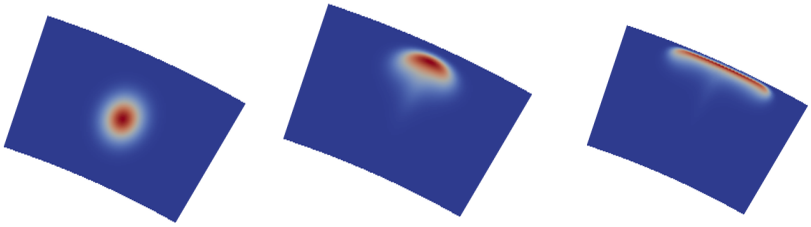

Figure 3.15: Ascending temperature anomaly at 0 s, 3×10^9 s and 6×10^9 s.

Relaxation test

To test relaxation part of the problem a spectral code (spherical harmonics in lateral direction and finite differences in radial direction) was employed [Kihoulou, 2019]. We compare viscous relaxation of the surface topography of particular zonal harmonic degrees. The varied parameters are topography degree, boundary condition on bottom boundary (free slip or no slip) and viscosity (constant or temperature-dependent). All models were considered without ocean beneath the ice shell. Since we are only interested in relaxation, we solve Stokes problem only and energy balance is omitted. However, we prescribe temperature profile

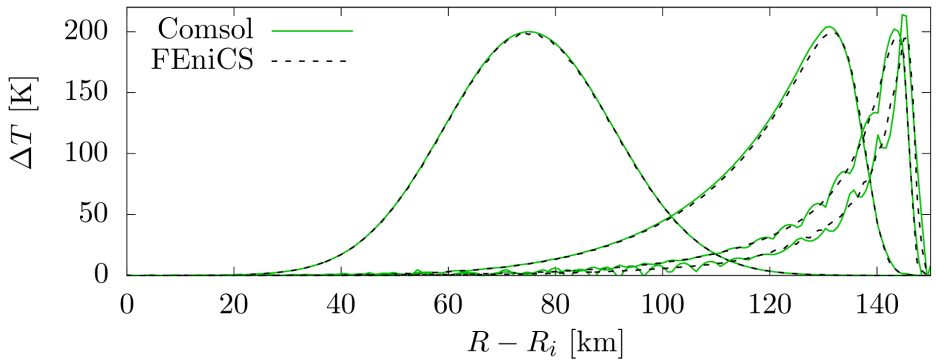

Figure 3.16: Radial temperature profile. From left: 0 s, 3×10^9 s, 6×10^9 s and 9×10^9 s.

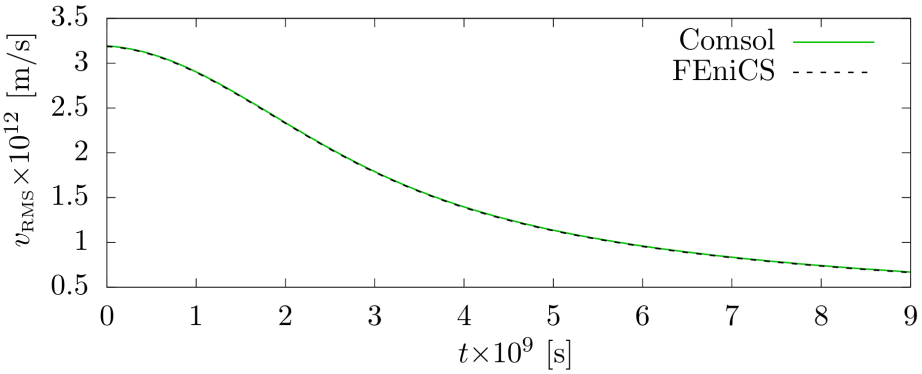

Figure 3.17: RMS velocity for convective test.

in order to define temperature-dependent viscosity

$$T(r) = T_{\mathrm{bot}} - (T_{\mathrm{bot}} - T_{\mathrm{top}}) \frac{r - R_i}{R_o - R_i}. \tag{3.60}$$

We tested top topography relaxation for degrees $j = 2, 5$ and 10 (see Figure 3.18), free or no slip bottom boundary condition and viscosity $10^{14}, 10^{17}, 10^{20}$ or temperature-dependent one given by Goldsby and Kohlstedt [2001]

$$\eta(T) = \frac{T d^2}{2A} \cdot \exp\left(\frac{E}{RT}\right), \tag{3.61}$$

where T is temperature, d is grain size, A is a parameter, E is activation energy and R is molar gas constant. For numerical reasons, cut-off viscosity 10^{24} is used.

Used models are summarized in Tables 3.4 and 3.5 and their parameters in Table 3.6.

Results

As a first type of results we will present relaxation curves, e.g. radial coordinate of a point at top boundary at symmetry axis with respect to time (denoted by blue point in Figure 3.18). This type of comparison will allows us to compare the effect of viscosity and topography degree.

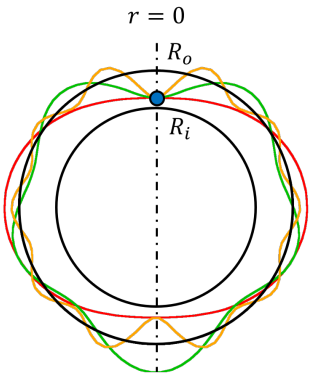

Figure 3.18: Geometry for the relaxation test. Surface topography of degree 2 (red), 5 (green) and 10 (orange) of spherical harmonics. Dashed line represents the axis of symmetry, blue point position will be used for the relaxation curve.

Model number	j	bottom BC	η [Pa · s]
1	2	free slip	10^{14}
2	2	no slip	10^{14}
3	5	free slip	10^{14}
4	5	no slip	10^{14}
5	10	free slip	10^{14}
6	10	no slip	10^{14}
7	2	free slip	10^{17}
8	2	no slip	10^{17}
9	2	free slip	10^{20}
10	2	no slip	10^{20}

Table 3.4: Models with η = const. used for relaxation test.

Model number	j	bottom BC	$\eta(T)$ [Pa · s]
11	2	free slip	$10^{14} - 10^{24}$
12	5	free slip	$10^{14} - 10^{24}$
13	10	free slip	$10^{14} - 10^{24}$
14	2	no slip	$10^{14} - 10^{24}$
15	5	no slip	$10^{14} - 10^{24}$
16	10	no slip	$10^{14} - 10^{24}$

Table 3.5: Models with $\eta = \eta(T)$ used for relaxation test.

Figure 3.19 shows the relaxation curves for constant viscosity $\eta = 10^{14}$ Pa · s for free slip (left) and no slip (right) boundary condition. Relaxation curves for other constant viscosities have the same shape, but they are shifted in time (Figure 3.20).

We observe that for constant viscosities and free slip condition there is no significant difference between relaxation timescales for different degrees j. In a zoomed window, we can see that relaxation time is increasing with increasing degree. However, if no slip condition prescribed, relaxation time increases with decreasing degree significantly.

Outer radius	R_o	1188	km
Ice shell thickness	H	327	km
Ice density	ρ_i	920	$\mathrm{kg \cdot m^{-3}}$
Parameter A	A	$9 \cdot 10^{-8}$	$\mathrm{Pa^{-1} \cdot s^{-1} \cdot m^2 \cdot K}$
Activation energy	E	59	$\mathrm{kJ \cdot mol^{-1}}$
Grain size	d	1	mm
Cut-off viscosity	$\eta_{\max}$	10^{24}	$\mathrm{Pa \cdot s}$
Gravity	g	0.617	$\mathrm{m \cdot s^{-2}}$
Elements in r	r_{div}	50	-
Elements in ϑ	ϑ_{div}	361	-

Table 3.6: Parameters for benchmark models

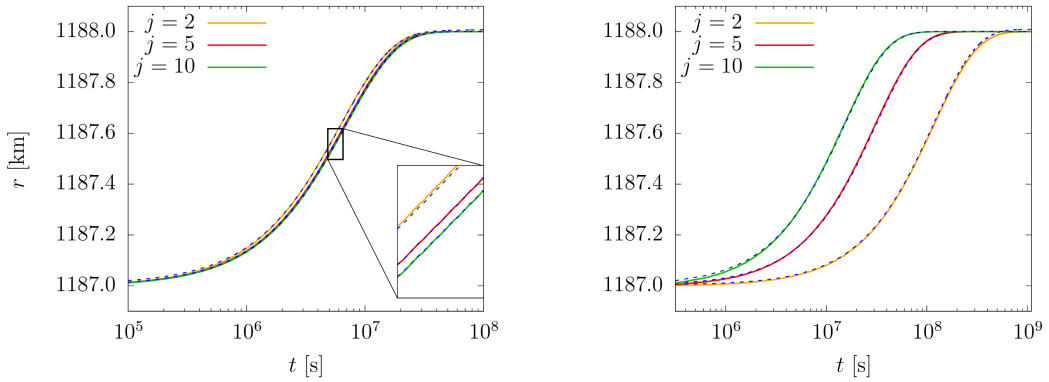

(a) Free slip condition.

(b) No slip condition.

Figure 3.19: Relaxation curves for $\eta = 10^{14}$ Pa · s. Fortran result is shown by a solid coloured line, FEniCS result by dashed line.

In case of temperature-dependent viscosity, the difference in relaxation time due to boundary condition is mostly suppressed by the viscous contrast, although the relaxation time for free slip is slightly shorter than for no slip (see Figure 3.21). The results of the test are very satisfactory.

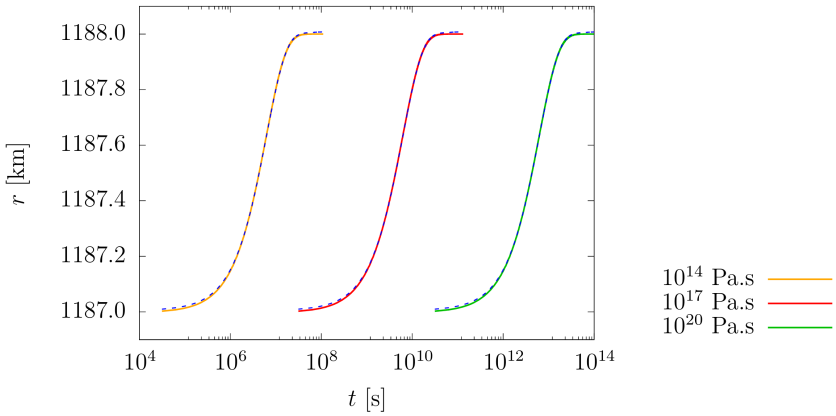

Figure 3.20: Relaxation curves for $j = 2$ and different viscosities. Fortran result is shown by a solid coloured line, FEniCS result by dashed line.

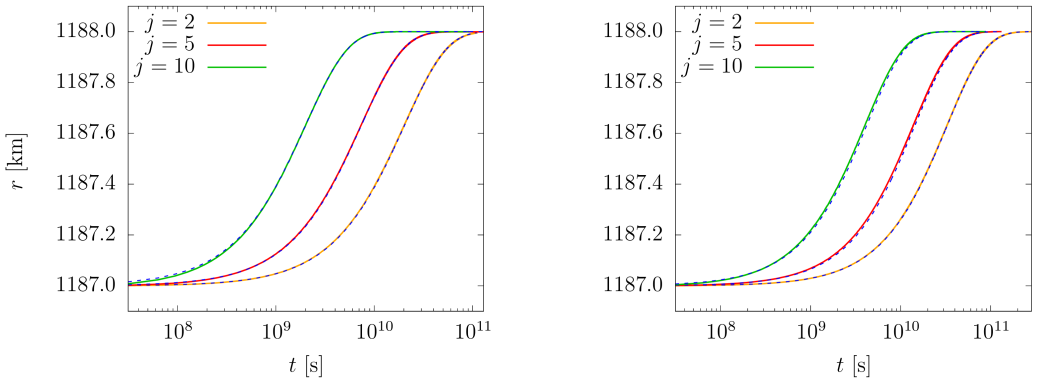

(a) Free slip condition.

(b) No slip condition

Figure 3.21: Relaxation curves for $\eta = \eta(T)$. Fortran result is shown by a solid coloured line, FEniCS result by dashed line.

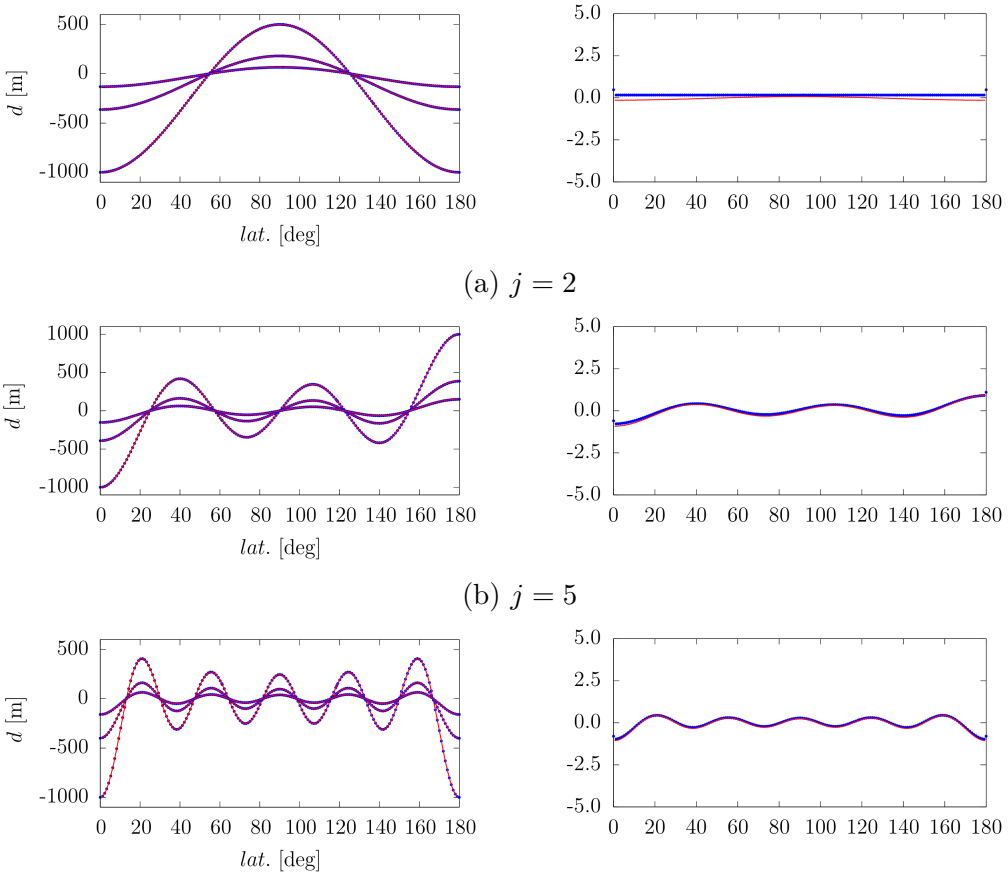

(a) $j = 2$

(b) $j = 5$

(c) $j = 10$

Figure 3.22: Relaxation of spherical harmonic degrees j by spectral method (red) and FEM (blue) for constant viscosity $\eta = 10^{14}$ Pa · s. Left column shows the initial condition and two timesteps of relaxation. Right column shows the end of the relaxation. Note different y axis range.

Figures 3.22 and 3.23 show relaxation of spherical harmonics on degrees 2, 5 and 10 for viscosity of 10^{14} Pa · s and temperature-dependent viscosity, respectively. Left pannels show initial condition and two other timesteps, while right

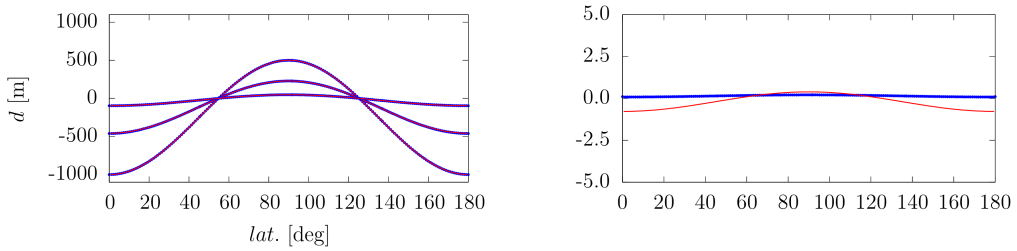

(a) $j = 2$

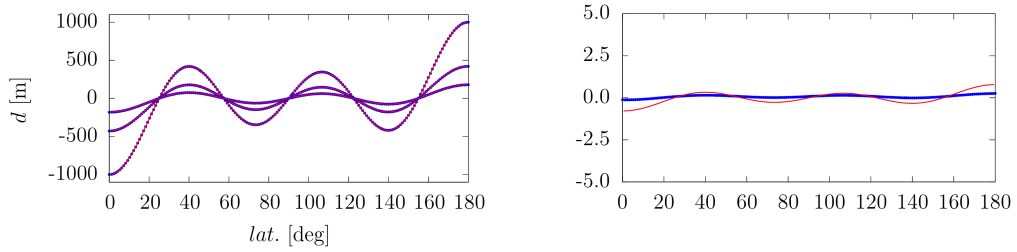

(b) $j = 5$

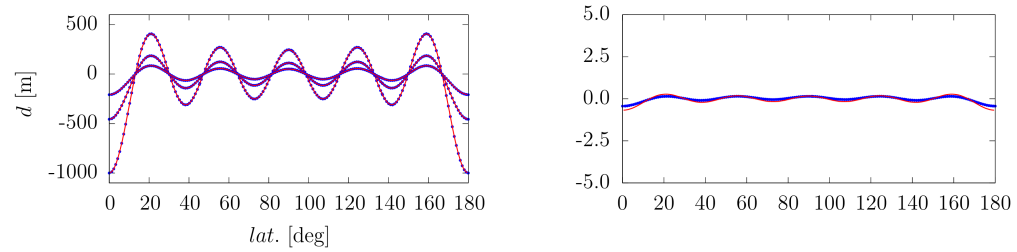

(c) $j = 10$

Figure 3.23: Relaxation of spherical harmonic degrees j by spectral method (red) and FEM (blue) for temperature dependent viscosity $\eta = \eta(T)$.

pannels show the values at the end of the relaxation curves. We see that the difference between the finite element and spherical harmonics solution is $\ll 1$ m.

Choosing crater shape for FEM

The aim of this test was to choose acceptable shape of a crater which would be described by an analytic function on a sphere. Figure 3.24 shows four functions used for crater description: cosine, gaussian, hyperbolic tangent and arctangent.

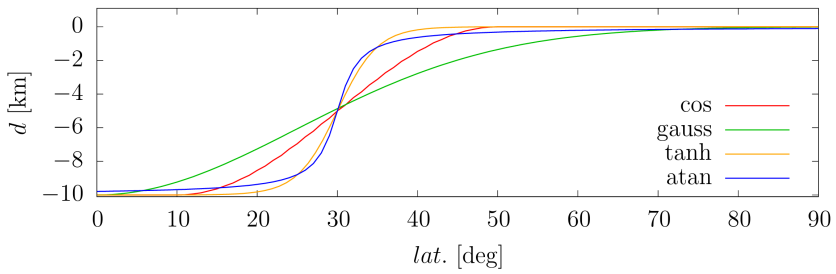

Figure 3.24: Different considered crater shapes.

However, in order to maintaining smoothness of the shape during the relaxation, it turned out to be necessary to describe the crater by only one smooth

function (i.e. not multiple functions with continuous derivatives, which is the case of *cos* prolonged by constant functions, see Fig 3.25).

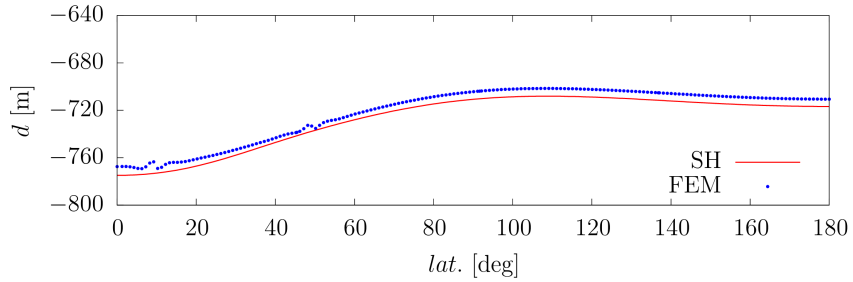

Figure 3.25: Discontinuity in cos-shaped crater.

We concluded that the best shape for crater is the hyperbolic tangent

$$h = -1000 \cdot \frac{1.0 + \tanh\left(\frac{\theta - 60}{10}\right)}{2}, \tag{3.62}$$

where θ is lattitude, meaning that the crater is situated at the north pole and has a radius of 30°. Although other proposed functions are also smooth, gaussian crater is not steep enough and arctangent decreases too slowly.

Crater relaxation test

The crater shape given by Equation (3.62) was decomposed in spherical harmonics in order to obtain its coefficients up to degree 20. Figure 3.26 compares crater shape evolution obtained by FEM and spectral method during relaxation at four instants. Note different ranges on y-axis.

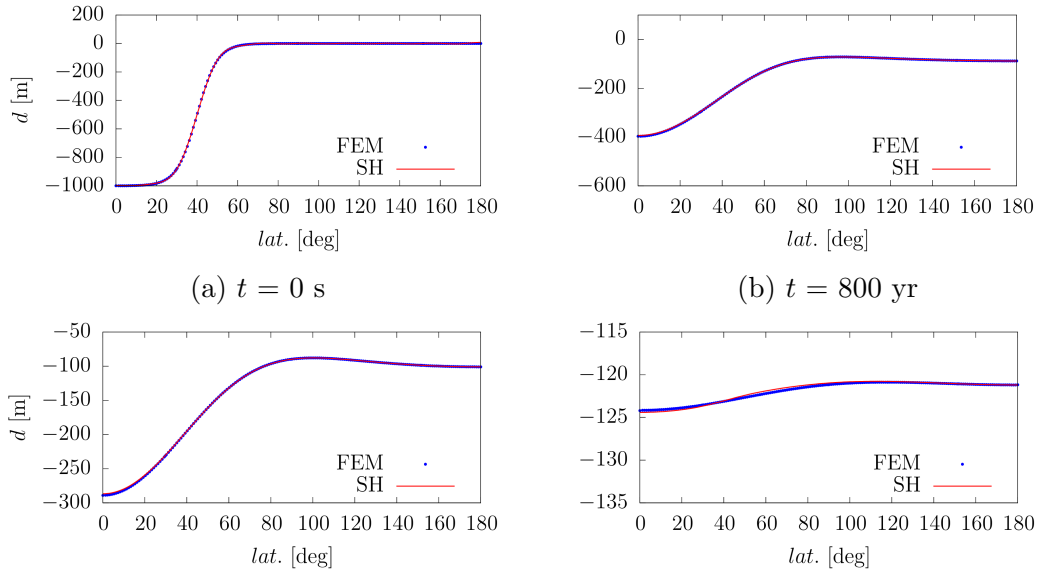

(a) $t = 0$ s

(b) $t = 800$ yr

(c) $t = 1100$ yr

(d) $t = 3800$ yr

Figure 3.26: Detail of crater relaxation. Note different scales at y axes.

We can clearly see that FEM solution maintains its smoothness over the relaxation process. The diffrence between FEM and SH method in the last frame is $\ll 1$ m, which is satisfactory result.

4. Crater relaxation modelling

This chapter is devoted to modelling of the viscous relaxation of Sputnik Planitia basin and its uplift with the spherical axisymmetric numerical model described in Chapter 3 and the impact parametrisation described in Chapter 2. First, we specify the material properties of ice, which, in Chapter 3, were simplified for the purpose of numerical tests, then we describe model settings. Finally, we present results for the uplift and surface crater relaxation.

4.1 Material properties of ice

So far, we have considered the ice viscosity to be dependent only temperature and grain size dependent, and ice thermal conductivity to be constant. However, in reality viscosity is also stress-dependent and thermal conductivity was found to be proportional to inverse temperature. In the following paragraphs, we will describe these dependences and discuss their numerical implementation.

Composite ice viscosity

Experiments show that there are several deformation mechanisms of ice flow, namely dislocation creep, basal slip (BS) and grain boundary sliding (GBS) [Goldsby and Kohlstedt, 2001]. Although diffusional flow was not observed, it is usually estimated using diffusion creep equations [Raj and Ashby, 1971]. These mechanisms are generally functions of temperature, grain size and stress and each mechanism is dominant in a different range of these parameters [Goldsby and Kohlstedt, 2001]. To describe the dislocation, GBS and BS regimes, following formula is used

$$\dot{\varepsilon} = A\frac{\sigma^n}{d^p}\exp\left(-\frac{Q}{RT}\right), \tag{4.1}$$

where A is a preexponential factor, d is grain size and p its exponent, σ is a differential stress and n its exponent, R the molar gas constant, Q the activation energy and T the temperature.

Since strain rate is a tensor quantity, we use its second invariant to evaluate its magnitude

$$\dot{\varepsilon}_{\mathrm{II}} = \sqrt{\dot{\varepsilon} : \dot{\varepsilon}/2}. \tag{4.2}$$

In terms of the velocity, in Cartesian coordinates we get

$$\dot{\varepsilon}_{\mathrm{II}} = \sqrt{\frac{1}{8}(\nabla\boldsymbol{v} + \nabla^T\boldsymbol{v}) : (\nabla\boldsymbol{v} + \nabla^T\boldsymbol{v})}, \tag{4.3}$$

and in axisymmetric cylindrical coordinates

$$\dot{\varepsilon}_{\mathrm{II}} = \sqrt{\frac{1}{8}\left[(\nabla\boldsymbol{v} + \nabla^T\boldsymbol{v}) : (\nabla\boldsymbol{v} + \nabla^T\boldsymbol{v}) + 4\frac{v_r^2}{r^2}\right]}. \tag{4.4}$$

The strain rate and stress invariants are then related through viscosity

$$\eta = \frac{\sigma_{\mathrm{II}}}{2\dot{\varepsilon}_{\mathrm{II}}}. \tag{4.5}$$

Substituting this relation into (4.1), we can express viscosity as

$$\eta_i = \frac{1}{2} A^{-1/n_i} d^{p_i/n_i} \dot{\varepsilon}_{\mathrm{II}}^{(1-n_i)/n_i} \exp\left(\frac{Q}{n_i RT}\right), \tag{4.6}$$

where i denotes the particular creep mechanism, $i \in \{\mathrm{disl}, \mathrm{GBS}, \mathrm{BS}\}$. At high temperatures ($T > 258$ K for dislocation creep, $T > 255$ K for GBS), large increase in strain rate is caused by premelting.

Diffusion creep is described by a relation that combines volume and grain boundary diffusion

$$\eta_{\mathrm{diff}} = \frac{RTd^2}{84V_m}\left(D_v + \frac{\pi\delta}{d}D_b\right)^{-1}, \tag{4.7}$$

$$\begin{aligned} D_v &= D_{0,v}\exp\left(-\frac{Q_v}{RT}\right), \\ D_b &= D_{0,b}\exp\left(-\frac{Q_b}{RT}\right), \end{aligned} \tag{4.8}$$

where V_m is molar volume, δ is grain boundary width and $D_{0,v}$ and $D_{0,b}$ along with Q_v and Q_b denote preexponential factor and activation energy for volume diffusion and grain boundary diffusion, respectively. Diffusion creep is the only stress-independent mechanism. Parameters for these mechanisms are summarized in Tables 4.1 and 4.2.

Creep regime	A ($\mathrm{Pa}^{-n}\cdot\mathrm{m}^p\cdot\mathrm{s}^{-1}$)	n	p	Q ($\mathrm{kJ}\cdot\mathrm{mol}^{-1}$)
Dislocation ($T < 258$ K)	$4.0\cdot10^{-19}$	4.0	0.0	60
Dislocation ($T > 258$ K)	$6.0\cdot10^{4}$	4.0	0.0	180
GBS ($T < 255$ K)	$6.2\cdot10^{-14}$	1.8	1.4	49
GBS ($T > 255$ K)	$5.6\cdot10^{15}$	1.8	1.4	192
BS	$2.2\cdot10^{-7}$	2.4	0.0	60

Table 4.1: Parameters for dislocation creep, grain boundary sliding and basal slip [Goldsby and Kohlstedt, 2001].

Viscosities obtained by Equations (4.6) and (4.7) are then combined by the following formula, e.g. [Goldsby and Kohlstedt, 2001]

$$\frac{1}{\eta_{\mathrm{eff}}} = \frac{1}{\eta_{\mathrm{diff}}} + \frac{1}{\eta_{\mathrm{disl}}} + \frac{1}{\eta_{\mathrm{GBS}} + \eta_{\mathrm{BS}}} + \frac{1}{\eta_{\max}}, \tag{4.9}$$

where η_{eff} is called effective viscosity and we introduced the cut-off viscosity $\eta_{\max}$ which bounds the viscosity from above for numerical reasons. Ice viscosity at ice/ocean interface is approximately $10^{14}-10^{15}$ Pa·s while at surface of icy bodies, because of low temperatures, deformation mechanisms give enormous viscosity (e.g. $> 10^{30}$ Pa $\cdot$ s). Such high viscosities cause problems with numerical solution and also stresses much higher than yield stress of ice. It is thus convenient to bound viscosity from above to reduce the viscous contrast. Values of cut-off viscosity are usually in the range of $10^{22} - 10^{30}$ Pa $\cdot$ s.

Parameter		Value	Unit
Molar volume	V_m	$1.97 \cdot 10^{-5}$	m^3
Volume diffusion			
Prefactor	$D_{v,0}$	$9.1 \cdot 10^{-4}$	$\mathrm{m}^2 \cdot \mathrm{s}^{-1}$
Activation energy	Q_v	59.4	$\mathrm{kJ} \cdot \mathrm{mol}^{-1}$
Grain boundary diffusion			
Prefactor	$D_{b,0}$	$6.4 \cdot 10^{-4}$	$\mathrm{m}^2 \cdot \mathrm{s}^{-1}$
Activation energy	Q_b	49	$\mathrm{kJ} \cdot \mathrm{mol}^{-1}$
Grain boundary width	δ	$9.04 \cdot 10^{-10}$	m

Table 4.2: Parameters for diffusion creep [Goldsby and Kohlstedt, 2001].

The choice of this value of course must not affect the result. For typical shell temperatures of icy bodies, cut-off viscosity is reached tens of kilometres below surface. Relaxation of surface topography (impact crater) is then determined by our choice of the cut-off, thus a purely viscous approach is not appropriate. Plasticity should be introduced due of high stresses and elasticity for long-term support of the topography.

Thermal conductivity

We will use temperature-dependent conductivity given by Hobbs [2010]

$$k(T) = \frac{488.12}{T} + 0.4685. \tag{4.10}$$

Because thermal conductivity is proportional to the inverse of temperature, the highest conductivity will be at cold surface, while the lowest at the bottom of the shell.

Numerical implementation

Since the ice viscosity is now strain-rate dependent (i.e. velocity dependent), the momentum balance (3.2) becomes nonlinear in velocity. We deal with this by employing Picard iterations [Logg et al., 2012, Alnæs et al., 2015].

We linearise the momentum equation by using known velocity $\boldsymbol{v}^k$ from the previous timestep. Then we iterate the solution. We are evaluating velocity norm $||\boldsymbol{v}||$ for all nodes in the domain and check how the solution is converging (e.g. if the ratio $||\boldsymbol{v}||/||\boldsymbol{v}_k||$ converges to 1). Iterations end when the solution is sufficiently improved or when the maximum number of iterations is reached.

For temperature-dependent thermal conductivity given by Equation (4.10), energy balance becomes nonlinear in temperature. Since we do not expect any high temperature changes, we use a value of T^k from the previous time step, however, without any iterations.

4.2 Uplift relaxation

In this section we will investigate the relaxation of the isostatic uplift beneath Sputnik Planitia basin. Since it compensates the negative gravity topography, its relaxation timescale is crucial for the reorientation theory.

4.2.1 Model settings

Clathrate hydrate layer

Clathrate layer was introduced in Chapter 1 as a possible mechanism to prolong the relaxation time of the ice shell. Here we will discuss its properties and effects in more detail.

Clathrate hydrates are water-based solids which have gas molecules trapped in the ice crystal lattice. Typical gas molecules are methane, ethane, nitrogen or carbon oxide. These compounds might form in a subsurface ocean, where volatile gasses are dissolved and, as they rise, they subsequently form a layer at the base of the ice shell [Choukroun et al., 2013]. The most promising option for the trapped gas is methane[1], whose traces were discovered at Pluto's surface [Grundy et al., 2016]. Based on laboratory experiments, they are believed to prevent the ocean from freezing and to slow down uplift relaxation substantially [Waite et al., 2006, Durham et al., 2003]. Below we will describe their thermal and mechanical properties and the resulting implications to shell dynamics.

To describe the position of clathrates at the bottom of the shell, we will use by the following function ϕ

$$\phi(R) = -\frac{1}{\pi}\arctan[0.002(R - (R_{in} + h_c + h))] + 0.5, \tag{4.11}$$

where R is radial distance, R_{in} inner shell radius, t_{cl} clathrate layer thickness and h bottom free surface height. See also Figure 4.1.

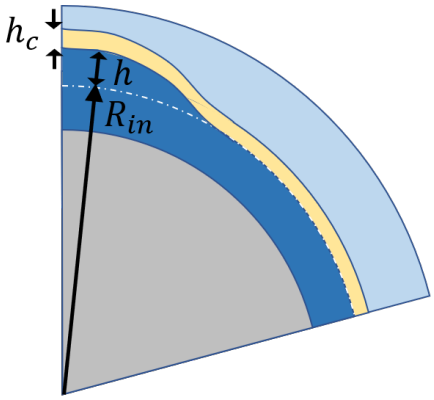

(a) Outwards: core, ocean, clathrates, ice shell.

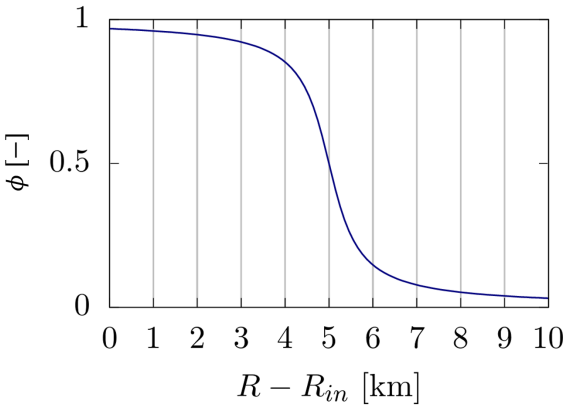

(b) Function ϕ.

Figure 4.1: Left: clathrate layer of uniform thickness. Right: clathrate concentration function ϕ for $h = 0$ and $h_c = 5$ km.

[1]Methane based clathrate is then methane-hydrate $CH_4 \cdot nH_2O$.

Thermal effect

Methane-clathrate has significantly lower thermal conductivity than water ice ($k_{\text{clathr}} = 0.5\ \text{W} \cdot \text{m}^{-1} \cdot \text{K}^{-1}$) [Waite et al., 2006]. It implies that the clathrate layer position can affect the thermal state and dynamics of the ice shell. If the layer is present at the base of the shell, it reduces the heat flux from the ocean and the shell cools down. In this case, thermal conductivity in the shell will be described by function ϕ in the following way

$$k(T, h) = k_{\text{ice}} + \phi(k_{\text{clathr}} - k_{\text{ice}}) \tag{4.12}$$

where k_{ice} is ice thermal conductivity given by Equation (4.10).

Kamata et al. [2019] argue that if this was the case of Pluto, the shell would be rigid and the uplift would relax slowly. Later we will show how the clathrate layer will affect the relaxation.

Pre-impact thermal state

Sputnik Planitia is expected to be 4 Gyr old [Greenstreet et al., 2015]. To simulate the uplift relaxation, we need to estimate thermal profile in the ice shell before the impact. Since methane clathrates cause the shell to cool down, we will be interested in cooling timescales. As an initial condition for cooling we will use conductive profile given by ice conductivity (Equation (4.10)). Then we solve the thermal evolution given by Equations (3.1) - (3.3) with conductivity given by Equation (4.12). To determine the cooling timescale, we evaluate the average shell temperature in every timestep. Cooling simulations were performed for a combination of 100 km or 200 km thick shell and 5 km or 10 km thick clathrate layer.

Figure 4.2 shows the evolution of average shell temperature with time. We observe that the shell of thickness 100 km is cooled down in 100 Myr, while the one of thickness 200 km in 300 Myr. Regarding the timescales of clathrate layer formation considered by Kamata et al. [2019] which are shorter than 100 Myr, these values are low enough to assume that the shell was cooled down before the impact.

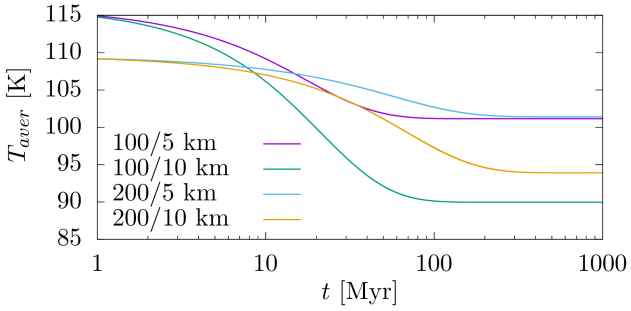

Figure 4.2: Ice shell cooling timescales. Key: ice shell thickness (km) / clathrate layer thickness (km).

Figure 4.3 shows steady-state temperature profiles without, with 5 km and with 10 km of clathrate layer and two ice shell thicknesses. We observe that cooling effect is stronger for the thinner shell.

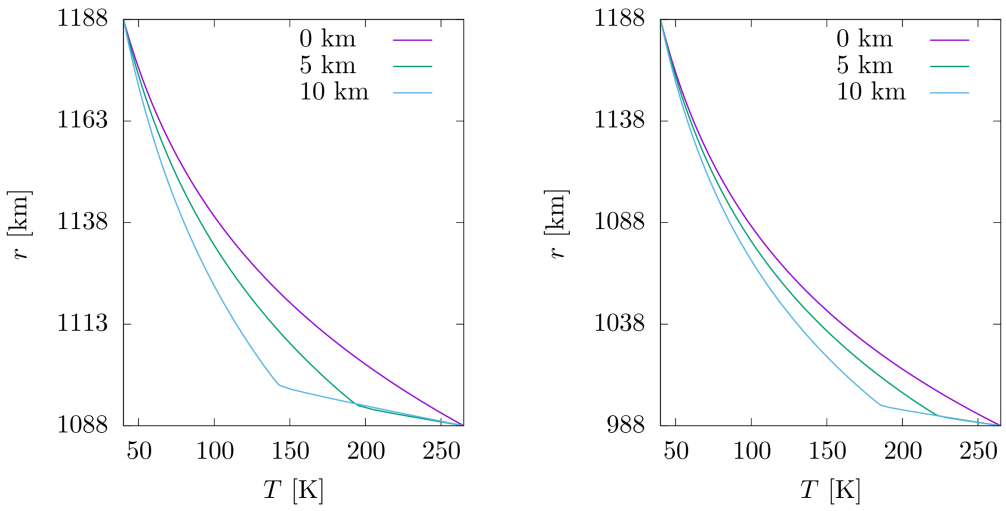

(a) Shell thickness 100 km.

(b) Shell thickness 200 km.

Figure 4.3: Conductive temperature profiles for clathrates layer thicknesses 0 km, 5 km and 10 km.

Mechanical effect

Clathrates deform by basal slip and have higher viscosity than water ice [Durham et al., 2003]. Viscosity spatial dependence will be again described by the function ϕ, however, since viscosity variations are of several orders of magnitude, we will use the following formula

$$\eta(T, v^k, \phi) = \eta_{\text{eff}}^{1-\phi} \eta_{\text{clath}}^{\phi}, \tag{4.13}$$

where the ice viscosity η_{eff} is given by Equation (4.9) and clathrates viscosity η_{clathr} by Equation (4.6) with the following parameters: $A = 2.24 \cdot 10^{-5}$ Pa$^{-2.2} \cdot$ s^{-1}, $n = 2.2$, $p = 0.0$ and $Q = 90$ kJ $\cdot$ mol^{-1}.

However, instead of Equation (4.6), Kamata et al. [2019] use viscosity of ice given by the following formula

$$\eta(T) = \eta_0 \exp\left[\frac{Q}{R}\left(\frac{1}{T} - \frac{1}{273.0}\right)\right], \tag{4.14}$$

where $\eta_0 = 10^{14}$ Pa $\cdot$ s is the viscosity at melting temperature, Q is the activation energy $Q = 60$ kJ $\cdot$ mol^{-1} and R is the gas constant. This formula, since it is stress-independent, gives slightly higher viscosity than Equation (4.6), which implies slower relaxation. Clathrates viscosity is also given by equation Equation (4.14) with parameters $\eta_0 = 2.0 \cdot 10^{14}$ Pa $\cdot$ s and $Q = 90$ kJ $\cdot$ mol^{-1}. This gives the viscosity of clathrates approximately one order of magnitude higher than that of water ice.

Ocean density and isostatic uplift

As Johnson et al. [2016] show, it is not possible to obtain positive gravity anomaly unless the ocean is denser than approximately 1100 kg $\cdot$ m^{-3}. Its density can be increased, e.g. by presence of $5 - 10\%$ of $MgSO_4$ [Hogenboom et al., 1995]. This

salt was found in both CI and CM chondrites, suggesting that it might be present in icy bodies cores and, thanks to its solubility, also in their oceans.

Based on an estimate of Nimmo et al. [2016a], we assume that the final basin was 10 km deep. Assuming Airy isostasy, the uplift topography is then given by a formula

$$h_{\mathrm{bot}} = -h_{\mathrm{top}} \frac{\rho_{\mathrm{i}}}{\rho_{\mathrm{w}} - \rho_{\mathrm{i}}} \frac{R_o^2}{R_i^2}, \tag{4.15}$$

where h_{top} is surface topography, ρ_{i} and ρ_{w} ice and ocean densities, respectively, and R_o and R_i outer and inner radii of the ice shell, respectively [Airy, 1855]. We assume that the change in gravity through the ice shell is negligible.

Impact parameters

We will estimate the impactor diameter using Equation (2.8) thanks to known dimensions of Sputnik Planitia basin, assuming escape velocity $v_{\mathrm{esc}} = 1.2\ \mathrm{km \cdot s^{-1}}$, target (Pluto's ice shell) density $\rho = 920\ \mathrm{kg \cdot m^{-3}}$, radius 1188 km and vertical impact $\cos(\theta) = 0$. Although Sputnik Planitia has an elliptical shape (probably caused by an oblique impact), we have to satisfy the axisymmetry, therefore we will assume a vertical impact and consider average radius of the basin.

Zahnle et al. [2003] estimated average impact velocity on Pluto of $1.9\ \mathrm{km \cdot s^{-1}}$. However, impact heating theory presented in Section 2.2 is valid only for impact velocities greater than elastic velocities of the target material. According to Kohnen [1974], P-wave velocity in ice is given by

$$v_P = -(2.3 \pm 0.17)T + 3795\ \mathrm{m \cdot s^{-1}}, \tag{4.16}$$

where T denotes temperature in degrees of Celsius. This result was obtained by fitting the data in temperature range (-10, - 60) °C. Extrapolating to Pluto's surface temperature 40 K, we get approximately $4300\ \mathrm{m \cdot s^{-1}}$, however, as the shell is getting warmer towards body interior, v_P is decreasing to the value $3795\ \mathrm{m \cdot s^{-1}}$ at the ice/ocean interface.

Figure 4.4 shows the dependence of the final crater diameter on the impactor diameter, its velocity and density. By assuming icy ($\rho_{\mathrm{imp}} = 920\ \mathrm{kg \cdot m^{-3}}$) or rocky ($\rho_{\mathrm{imp}} = 3300\ \mathrm{kg \cdot m^{-3}}$) impactor and impact velocities $2, 3$ or $4\ \mathrm{m \cdot s^{-1}}$, we try to find parameters consistent with Sputnik Planitia minimal diameter 900 km.

Although several combinations of impactor parameters satisfy final crater diameter, we choose an icy impactor of diameter 400 km and impact velocity $4\ \mathrm{km \cdot s^{-1}}$. To fulfil the assumption for shock wave development, we prefer higher impact velocity. Rocky impactor of such velocity would create too large crater, so we choose an icy impactor with lower density. Since Denton et al. [2020] used impactors of 350 - 450 km in diameter, our choice of 400 km is reasonable. Temperature anomaly resulting from Equation (2.7), assuming $\gamma = 0.4$, is approximately 86 K.

Computed models

Figure 3 in Kamata et al. [2019] shows how the thickness of the clathrate hydrate layer prolongs the relaxation time. We observe that the maximum efficiency lies in the range from 5 to 10 km, depending on the shell thickness. We thus decided

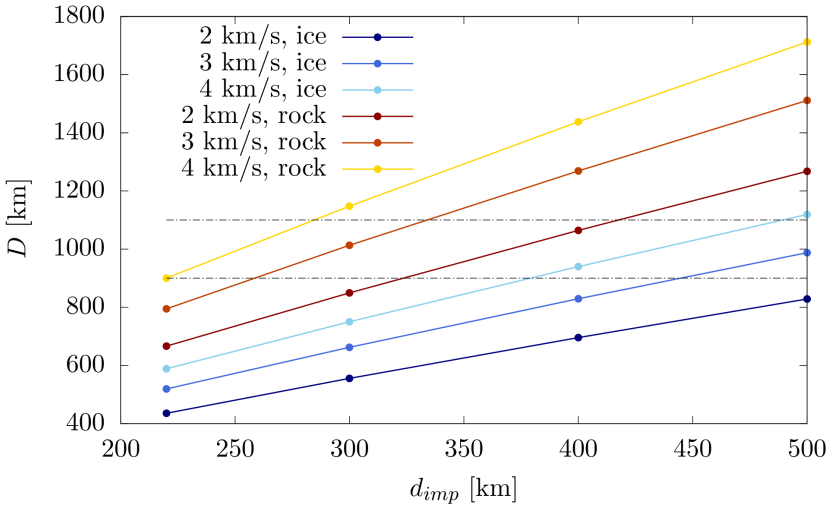

Figure 4.4: Dependence of final crater diameter D on impactor diameter d_{imp}, velocity and density. Dashed lines indicate the minimal and the maximal diameters of Sputnik Planitia basin.

to combine these two clathrate thicknesses and shell thicknesses 100, 150 and 200 km.

At first, we investigate the effect of ice shell thickness H (models 1, 2 and 3) assuming that there is no clathrate layer. Then, for thickness $H = 150$ km we study the effect of clathrate hydrate layer ($h_c = 5$ and 10 km, models 4 and 5). Finally, we compute the longest-lasting relaxations of Kamata et al. [2019], which are combinations $H/h_c = 100/5$km and $H/h_c = 200/10$km. Models 6 and 7 (with Newtonian rheology, without both impact heating and thermal evolution[2]) should reproduce the results of Kamata et al. [2019]. Then we add thermal evolution (models 8, 9) and impact heating with composite rheology (models 10, 11). All initial conditions are conductive states, disregarding whether convection can or cannot develop (particularly for Models 1-3). Table 4.3 summarizes all parameters for Sputnik Planitia uplift relaxation problem and Table 4.4 summarizes computed models.

4.2.2 Results

We are assuming that the ocean uplift isostatically compensates the surface basin Sputnik Planitia and that the positive gravity required for reorientation is provided by ejecta blanket and the nitrogen layer. Since it takes only a few kilometres of uplift subsidence for gravity to change its sign, the crucial moment is rather the start than the end of the relaxation process. We try to find the model for which the shell can be maintained unrelaxed in the order of billions of years.

Effect of ice shell thickness

First, we investigated the effect of ice shell thickness. Table 4.5 summarizes the varied parameters and the results. By relaxation start we mean the moment when

[2]Viscosity profile in Kamata et al. [2019] is evaluated only from the pre-impact thermal state and does not evolve in time.

Outer radius	R_o	1188	km
Gravity	g	0.617	$\mathrm{m \cdot s^{-2}}$
Ice shell thickness	H	100, 150, 200	km
Clathrate layer thickness	h_c	0, 5, 10	km
Ice density	ρ_i	917	$\mathrm{kg \cdot m^{-3}}$
Water density	ρ_w	1100	$\mathrm{kg \cdot m^{-3}}$
Surface temperature	T_{top}	40	K
Ice/ocean interface temperature	T_{bot}	265	K
Grain size	d	1	mm
Cut-off viscosity	η_{cut}	10^{24}	$\mathrm{Pa \cdot s}$
Impactor velocity	v_{imp}	4	$\mathrm{km \cdot s^{-1}}$
Impactor diameter	d_{imp}	400	km
Impactor density	ρ_{imp}	920	$\mathrm{kg \cdot m^{-3}}$
Impact heating efficiency	γ	0.4	–

Table 4.3: Parameters for Sputnik Planitia uplift relaxation.

Model number	H [km]	h_c [km]	rheology	Imp. heating	Thermal evol.
Shell thickness effect					
1	100	0	comp.	yes	yes
2	150	0	comp.	yes	yes
3	200	0	comp.	yes	yes
Clathrate layer thickness effect					
4	150	5	comp.	yes	yes
5	150	10	comp.	yes	yes
Setting of Kamata et al. [2019]					
6	100	5	newt.	no	no
7	200	10	newt.	no	no
8	100	5	newt.	no	yes
9	200	10	newt.	no	yes
10	100	5	comp.	yes	yes
11	200	10	comp.	yes	yes

newt. = Newtonian, Equation (4.14)
comp. = composite, Equation (4.6)

Table 4.4: Computed models.

the uplift centre visibly starts to descend (i.e. when the relaxation curve starts to point down).

As we can see from the initial conditions, the shell of thickness 100 km (Figure 4.5a) has the highest uplift/shell thickness ratio[3]. This implies that the uplift is close to the cold surface, and thus the impact thermal anomaly cools quickly, resulting in weaker effect on viscosity decrease. This might be the reason

[3]This is caused by the $\sim (R_o/R_i)^2$ dependence of uplift height in Equation (4.15).

why this model shows the slowest relaxation.

Since viscosity is strongly temperature dependent, the lowest viscosity is where the shell is the warmest - at the base of the shell. This implies that the uplift will be filled by warm ice flowing along the shell base. Figure 4.5b shows the very moment when the crater becomes relaxed (i.e. when the relaxation curve reaches its minimum). At this moment, the warm ice is convecting.

Figure 4.5c shows that when the relaxation is over, shell cools down and convection declines.

H [km]	h_{bot}/H [km]	Relaxation start [Myr]	Convection
100	0.61	10^{-3}	local, declining
150	0.45	10^{-4}	global
200	0.38	10^{-5}	global

Table 4.5: Effect of shell thickness H on relaxation timescale and thermal evolution.

Figure 4.6 shows similar sets of snapshots for ice thicknesses 150 and 200 km, respectively. Compared to Model 1, these models have lower uplift/shell thickness ratio implying that there is thicker shell above the uplift to be heated by the postimpact thermal anomaly. Since there is more warm ice and another warm ice flows along the shell's base from lower lattitudes, the resulting convection is more vigorous. However, these shells are thick enough to develop convection even in regions outside the initial temperature anomaly as we can see in Figure 4.6c.

Relaxation curves (Figure 4.7) show that in all three cases the uplift relaxation is complete before 10 Myr, which makes it impossible to compensate the surface crater negative anomaly up to the present. Moreover, convection in the ice shell (Models 2 and 3) would probably cause ocean to freeze since it makes heat transfer more efficient than conduction only. Therefore, these models are not in agreement with the reorientation theory. For this reason, Kamata et al. [2019] proposed the presence of insulating, high viscosity clathrate layer at the ice/ocean interface to slow down the relaxation process.

Effect of clathrate layer thickness

As we showed in Figure 4.3, the layer of clathrate hydrates cools down the shell, thus increases ice viscosity. In addition, the viscosity of the clathrate layer itself is higher than the ice viscosity. Combination of these two effects results in slower relaxation.

Figure 4.8 shows initial viscosity fields (left column) and viscosity fields when the relaxation starts (right column). In Figure 4.8a we can see that if clathrate layer is not present (i.e. Model 2), the ice shell is warm and at the bottom there is a thick layer of warm ice of low viscosity. As we saw in Figure 4.6, this case leads to quick relaxation.

Figure 4.8b shows the case with 5 km of clathrates. It is clearly visible that viscosity at the very bottom of the shell is at least one order of magnitude higher than in the previous case. We observe that at the time of relaxation start, impact temperature anomaly is still present, decreasing the viscosity in the isobaric core.

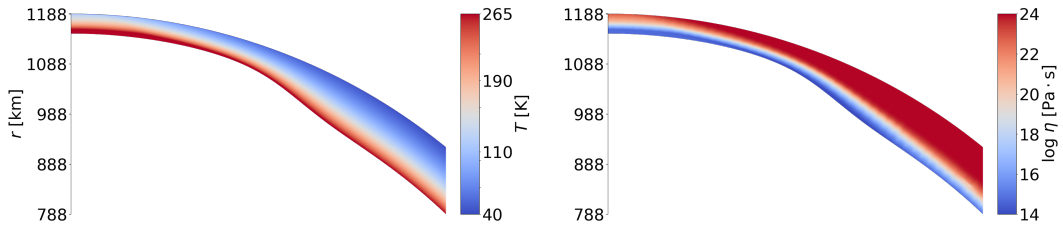

(a) Initial condition

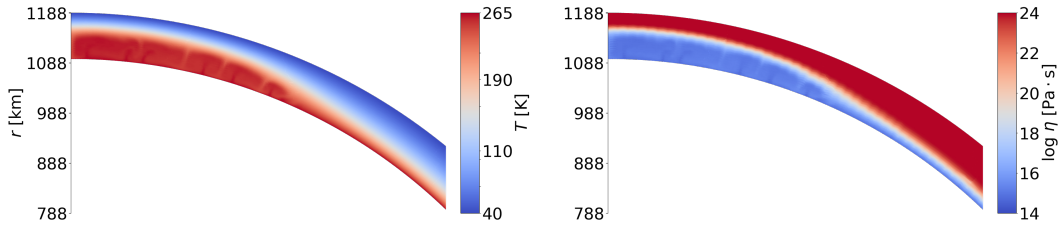

(b) $t = 5$ Myr

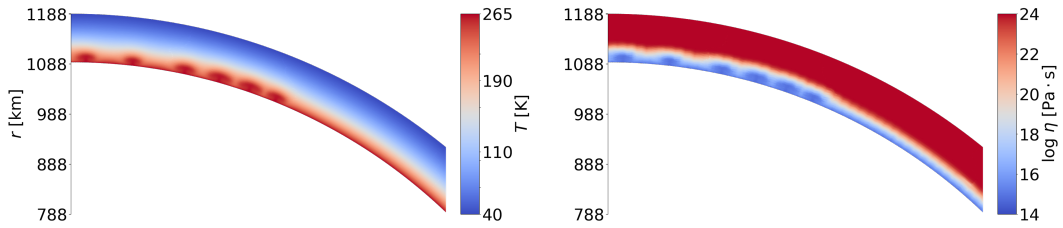

(c) $t = 1500$ Myr

Figure 4.5: Temperature (left) and viscosity (right) fields for Model 1 ($H = 100$ km). Convection in (b) is caused by infilling the uplift by warm ice. Later, convection declines (c).

Therefore, the shell is still warm enough to relax quickly (see relaxation curves in Figure 4.9).

However, with 10 kilometers of clathrates, the situation is different. Due to low initial temperature in the shell, impact temperature anomaly cools down faster (since the thermal conductivity is proportional to the inverse of temperature, see Equation (4.10)). Therefore, when the relaxation starts, the temperature anomaly is already cooled down and rigid (see Figure 4.8c) and the relaxation proceeds much more slowly than in the previous cases. Relaxation curves for all three cases are shown in Figure 4.9. We see that for 5 km of clathrates the relaxation start is only delayed, however, for 10 km relaxation start is gradual and much more delayed than in the previous cases. Still, the relaxation starts at ~ 1 Gyr and it is therefore likely that even in this case, the reorientation towards the tidal axis would not be stable for long enough time.

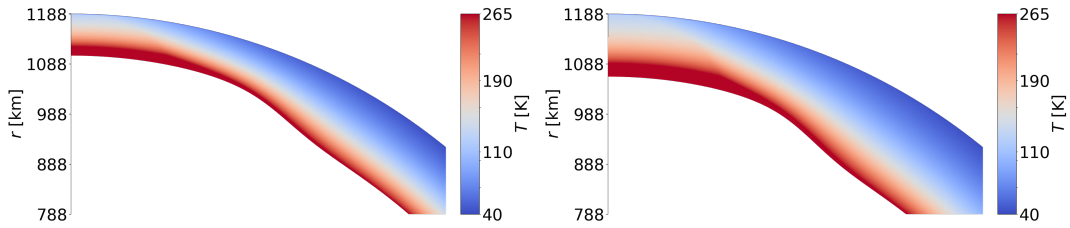

(a) Initial condition

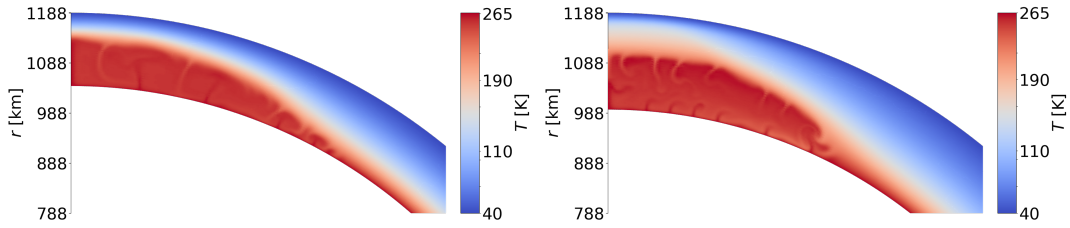

(b) End of the relaxation

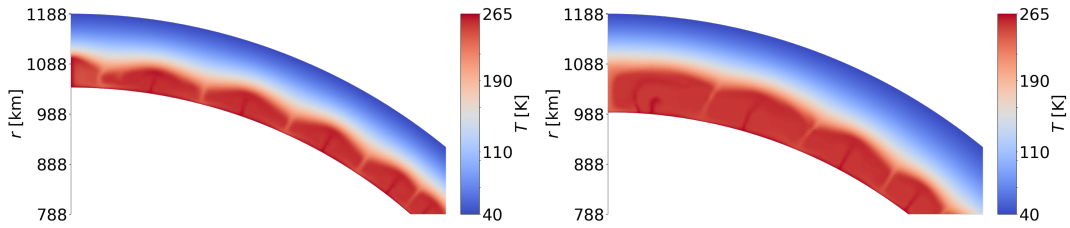

(c) Ongoing convection

Figure 4.6: Temperature profiles for Model 2 (left, $H = 150$ km) and Model 3 (right, $H = 200$ km). Due to increased shell thickness, isobaric core heats the shell more efficiently and relaxations start earlier. Both cases develop convection.

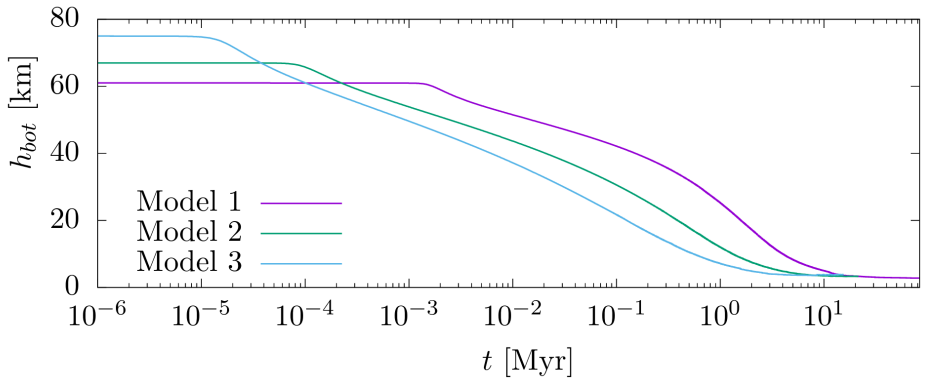

Figure 4.7: Relaxation curves for Models 1, 2 and 3 (shell thicknesses $H = 100$, 150 and 200 km). The thinner the ice shell is, the slower is the relaxation.

Setting of Kamata et al. [2019]

Here we investigate models with parameters $H/h_c = 100/5$ km (even model numbers) and $H/h_c = 200/10$ km (odd model numbers). Viscosity used in Kamata

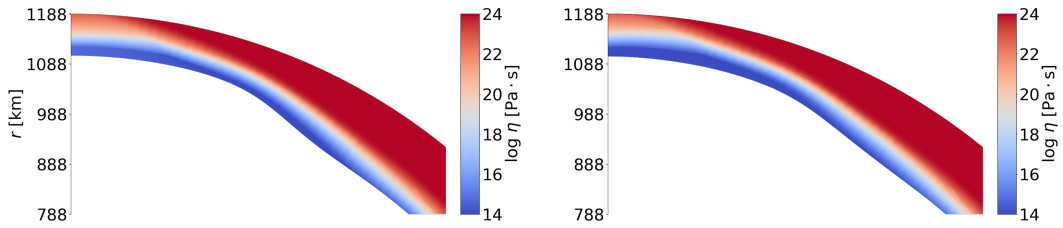

(a) $h_c = 0$ km

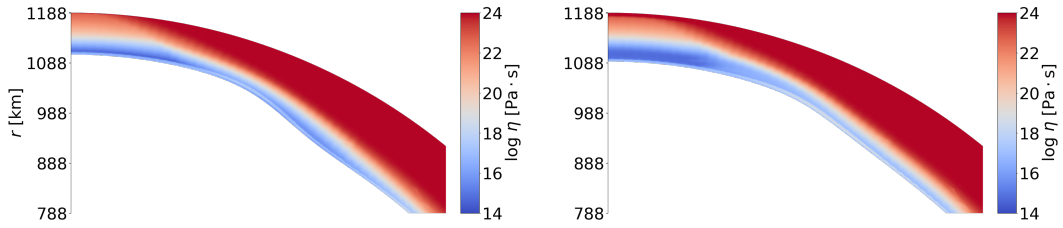

(b) $h_c = 5$ km

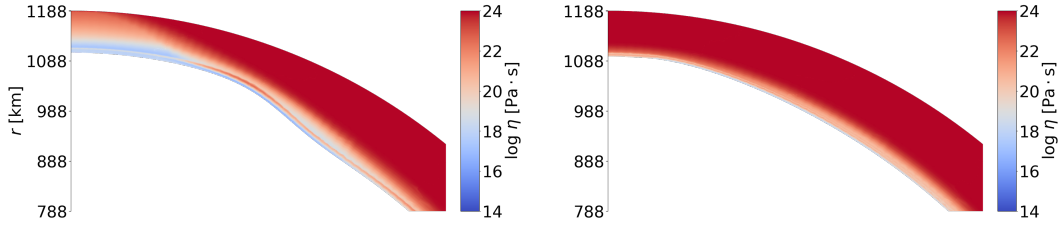

(c) $h_c = 10$ km

Figure 4.8: Viscosity profiles for Models 2, 4 and 5, top to bottom. Left column: initial condition, right column: relaxation start.

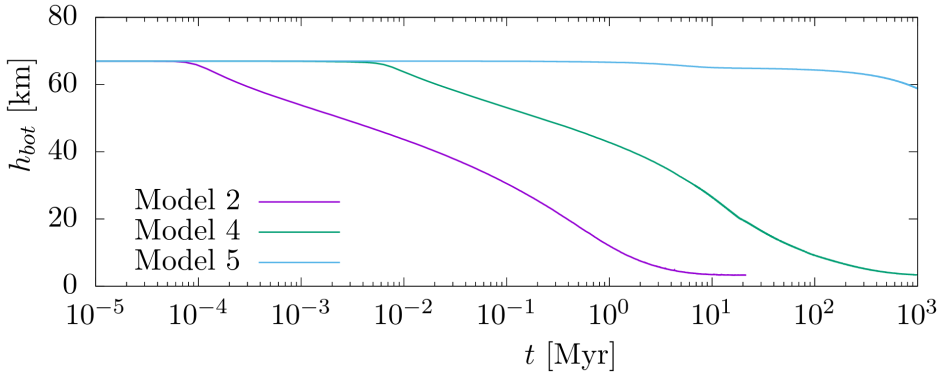

Figure 4.9: Relaxation curves for Models 2, 4 and 5 ($H = 150$ km, $h_c = 0$, 5 and 10 km).

et al. [2019] is only temperature dependent (for both ice and clathrates), also there is no impact thermal anomaly which would locally decrease viscosity (see viscosity profiles in Figure 4.10). To estimate the effect of these neglects, we

compare solutions with the same H and h_c, but different settings (viscosity, thermal evolution, temperature anomaly), see Table 4.4. We observe that there is no significant difference between Models 6, 7 (without thermal evolution) and 8, 9 (with thermal evolution). Because of high viscosity (and thus low velocities), heat is transfered only by conduction, resulting in stable thermal profile during the relaxation.

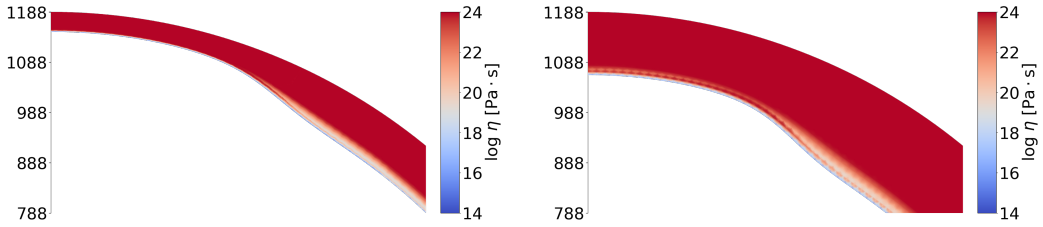

Figure 4.10: Initial viscosity profiles for Models 6,8 (left) and 7, 9 (right).

Figure 4.11 shows viscosity profiles for Models 10 and 11. The difference with respect to previous models is the inclusion of postimpact temperature anomaly and the stress dependence of viscosity. Thanks to these differences, the initial viscosity in the uplift region is substantially lower. Model 10 with a thin shell, however, relaxes slowly and the impact anomaly cools down quickly. This ressembles Figure 4.8c, however in this case the effect is even stronger thanks to the thinner shell. In Figure 4.11b (left) we can see how the area of locally decreased viscosity is proceeding towards the symmetry axis.

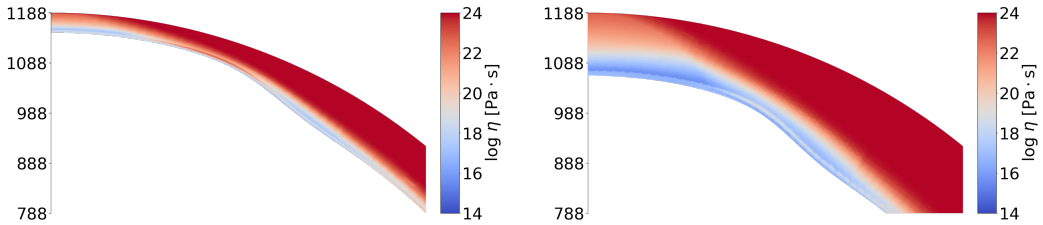

(a) Initial condition for Models 10 (left) and 11 (right).

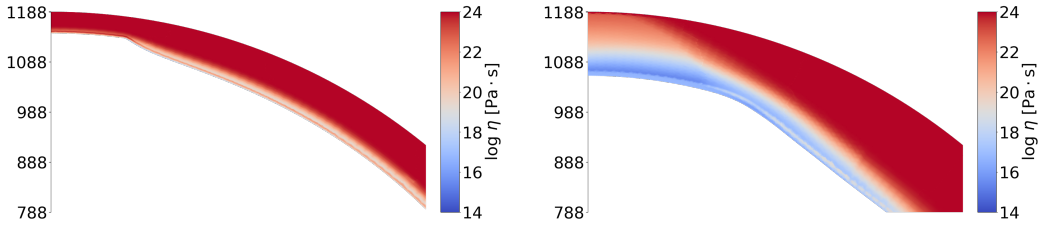

(b) Relaxation start for Models 10 (left) and 11 (right).

Figure 4.11: Viscosity profiles for Models 10 and 11. Top row: initial condition, bottom row: relaxation start.

Due to a thicker shell, Model 11 starts relaxing before the temperature anomaly is cooled down (Figure 4.11b). Although it cools down later and relaxation slows down, it is substantially faster than the models of Kamata et al. [2019] without temperature anomaly and nonlinear rheology.

Even though the thinner shell (Model 10) is cooled down in the moment of the relaxation start, stress-dependent viscosity speeds up the relaxation. Figure 4.12 shows that about 1 Gyr, the relaxation started, therefore long-term stability of the uplift is very unlikely even in the case of cold, thin shell.

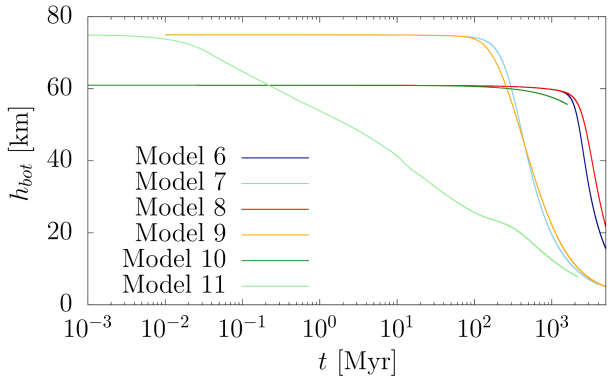

Figure 4.12: Relaxation curves for Models 6 – 11. Models with impact temperature anomaly and stress-dependent viscosity (Models 10 and 11) relax faster than models of Kamata et al. [2019] without these properties.

4.3 Surface crater relaxation

Throughout the Solar System, impact craters are in various stages of degradation. In general, degradation is caused by a combination of relaxational and erosional processes, such as volcanic outflows, sublimation deposits or tectonics, even on airless bodies. Viscous relaxation, which is investigated in this section, is therefore only an estimate of the crater's shape evolution.

Here, we do not simulate any particular crater, hence the results have rather qualitative character and should be regarded as a parametric study. We will investigate the effect of impactor size, which determines both the final crater diameter and the size of the isobaric core, and the effect of shell thickness.

4.3.1 Model settings

Impactor radius and shell thickness

If we consider fixed impactor density and velocity, the impactor radius determines the radius of the isobaric core and the radius of the final crater. We will assume a single final crater depth of 10 km for all models. The temperature anomaly, if sufficiently large, can speed up the relaxation. Since the volume of the surface

crater is proportional to $r_{\mathrm{imp}}^{\sim 1.5}$ (see Equation (2.8)), while the volume of the isobaric core is proportional to $3r_{\mathrm{imp}}^3$, we can expect the influence of the temperature anomaly increases with crater radius.

In this setting (surface crater), there is no thin warm layer, where the ice would fill the crater by lateral flow, as was the case for most of the models in Section 4.2. Almost whole shell has uniform value of viscosity, which changes the style of crater infilling.

Effect of cut-off viscosity

In the previous chapter, we introduced the use of the cut-off viscosity. Its value was not crucial, because the relaxation was governed by viscosity at the ice/ocean interface, usually many orders of magnitude lower than the cut-off value. However, in the case of a surface crater, the relaxation is actually governed by the cut-off viscosity. This is the pitfall of using viscous rheology only. Real materials undergo also elastic and plastic deformation. Elastic deformation represents reversible, immediate reaction to applied stress, while plasticity describes irreversible material behaviour if the yield strength is exceeded. Both these mechanisms are essential in the case of planetary surfaces.

By choosing the value of cut-off viscosity, we deliberately determine the relaxation velocity. However, we will still be able to recognize major differences between the computed models.

Computed models

Table 4.6 summarizes the parameters used for crater relaxation on Pluto's surface. Note that, unlike in Section 4.2, we assume a completely frozen hydrosphere of thickness 327 km and bottom temperature 150 K, based on estimates of Robuchon and Nimmo [2011]. This choice is motivated by the attempt to estimate the maximum relaxation time of Pluto's surface crater. Since we assume that the ice shell lays on the rocky core, no slip condition will be used for the ice/core interface. Ice viscosity is given by Equation (4.14), thus it is temperature-dependent only. Also note that we used a different impactor parameters ($v_{\mathrm{imp}}, \rho_{\mathrm{imp}}$)

Models varying the impactor size are listed in Table 4.7. We vary the impactor size in order to get final crater diameters from 10 to 1000 km. For these models, we use postimpact heating and solve thermal evolution.

The last set of models focuses on shell thickness in order to show how it affects the crater relaxation (Table 4.8). We will use crater diameter $D = 500$ km and three hypothetical shell thicknesses $H = 150$, 300 and 450 km. In these cases, thermal evolution is solved, however, without the initial impact temperature anomaly.

4.3.2 Results

Effect of impactor size

Figures 4.13 and 4.14 show the effect of the impactor size. Left columns show initial temperature condition. Right columns show surface topography at four moments of relaxation: initial condition, 100 Myr, 1 Gyr and 5 Gyr.

Outer radius	R_o	1188	km
Gravity	g	0.617	$\mathrm{m \cdot s^{-2}}$
Icy shell thickness	H	327	km
Ice density	ρ_i	917	$\mathrm{kg \cdot m^{-3}}$
Surface temperature	T_{top}	40	K
Ice/core interface temperature	T_{bot}	150	K
Grain size	d	1	mm
Cut-off viscosity	η_{cut}	10^{24}	$\mathrm{Pa \cdot s}$
Impactor velocity	v_{imp}	2	$\mathrm{km \cdot s^{-1}}$
Impactor diameter	d_{imp}	400	km
Impactor density	ρ_{imp}	3300	$\mathrm{kg \cdot m^{-3}}$
Impact heating efficiency	γ	0.4	–
Initial basin depth	h_{ini}	10	km

Table 4.6: Parameters for surface craters relaxation.

Model number	D [km]	r_{imp} [km]	r_{ic} [km]
1	10	0.5	0.7
2	50	4	6
3	100	10	14
4	500	77	110
5	1000	185	267

Table 4.7: Model parameters for the effect of impactor size.

Model number	D [km]	H [km]
6	500	150
7	500	300
8	500	450

Table 4.8: Model parameters for the effect of shell thickness.

We can clearly observe that the smaller crater (10 km, Figure 4.13a) does not relax within 5 Gyr of evolution, while the two largest craters are already relaxed after 5 Gyr. In Figures 4.13d and 4.14, 100 Myr snapshot show that the relaxation is fastest at the axis of symmetry, right above the temperature anomaly. In these two cases (500 and 1000 km crater), temperature anomaly cooled down in 400 and 700 Myr, respectively, thus at 100 Myr it still forces the boundary to relax due to thermal buoyancy. Also, for these craters, a feature resembling a crater rim emerges at the crater edge. This should not be mistaken for actual crater rim. Rims are created during the excavation and modification phase of an impact, when the material in the contact zone is pushed downwards and away. From its nature, rim topography is strictly positive.

Relaxation curves for these models are shown in Figure 4.15. Obviously, the relaxation time decreases with increasing crater size, however, crater of diameter 500 km relaxes faster than crater of diameter 1000 km.

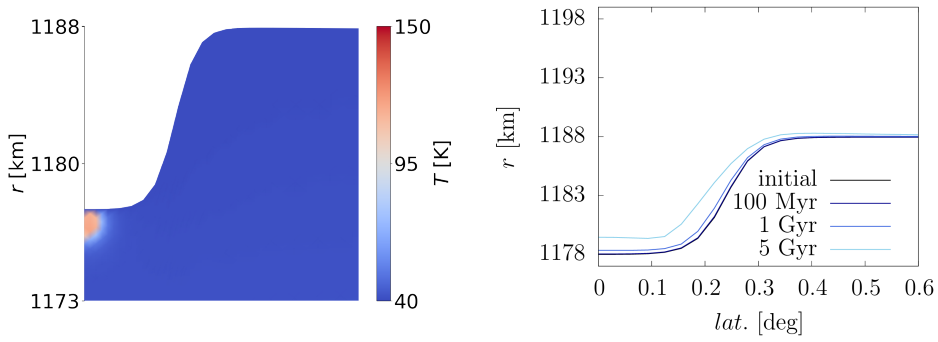

(a) $D = 10$ km

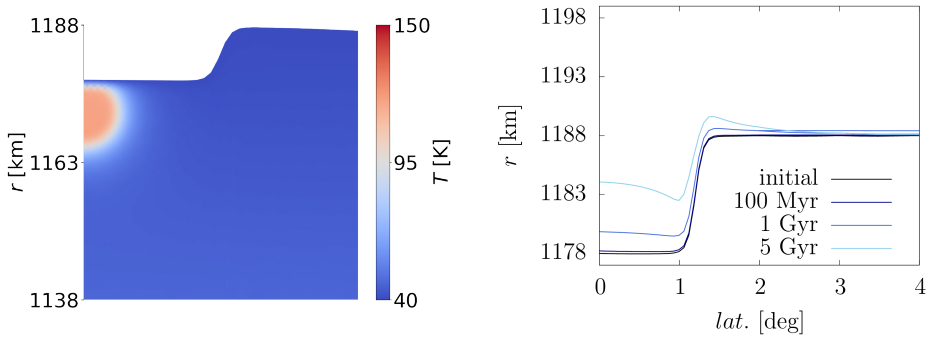

(b) $D = 50$ km

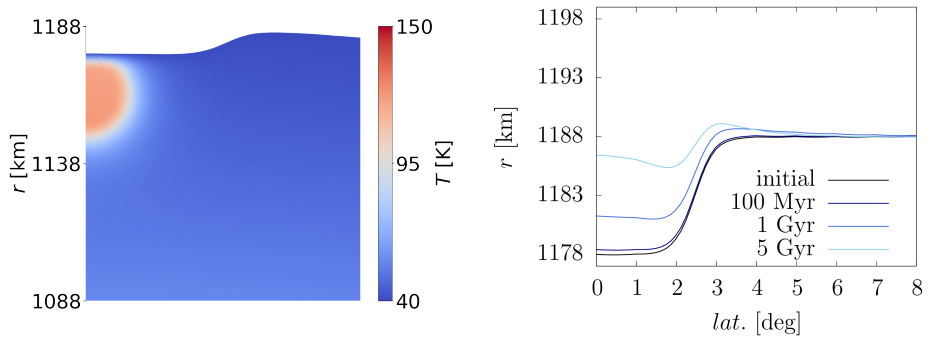

(c) $D = 100$ km

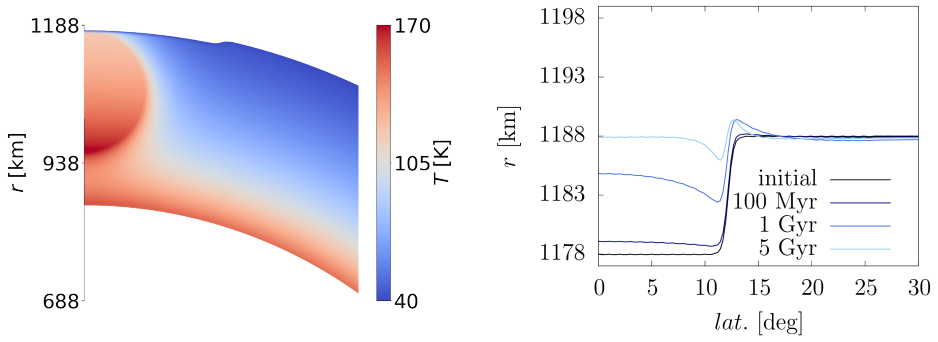

(d) $D = 500$ km

Figure 4.13: Initial temperature conditions (left) and snapshots of relaxation (right) for Models 1 – 4 ($D = 10$ – 500 km). Left boxes show $D \times D$ window, except of (a), which shows a 15×15 km window. Note a different temperature range in (d)

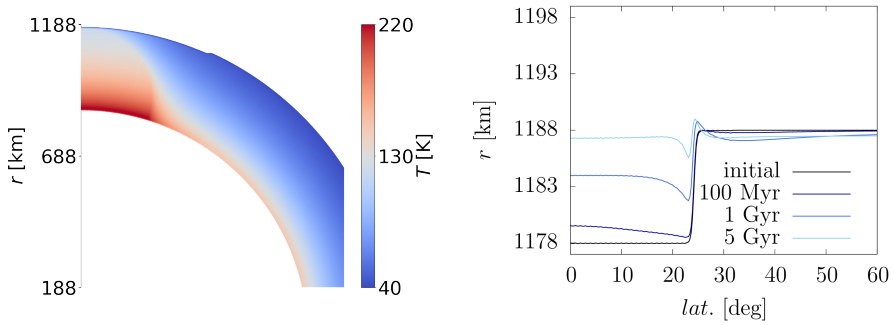

Figure 4.14: Initial temperature condition (left) and snapshots of relaxation (right) for Model 5 (D = 1000 km). Left box shows $D \times D$ window. Note that temperature range is different from the previous figure.

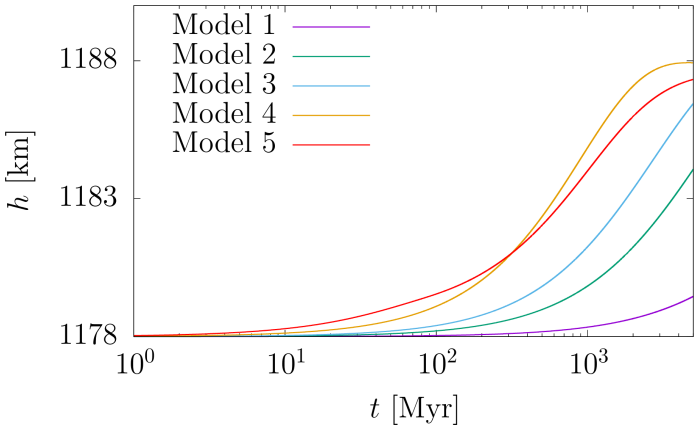

Figure 4.15: Relation curves for Models 1 – 5. Although relaxation time decreases with increasing crater site, the fastest relaxation does not surprisingly correspond to the largest crater.

Effect of shell thickness

Figure 4.16 shows velocity fields of two extreme cases (Models 6 and 8) at the beginning of the relaxation. The main difference lies in the radial component of the velocity v_r (left column). The former model, with a 150 km thick shell, has a maximum of the radial velocity near the crater edge, while the latter model, with a 450 km thick shell, has a maximum at the axis of symmetry.

We may explain this difference on the basis of the ratio of crater radius to shell thickness. Right panel of Figure 4.16 shows that the lateral flow is most pronounced around the crater edge in a domain comparable to shell thickness. If the crater radius is comparable with shell thickness, relaxation is fastest at the axis of symmetry. However, if the crater is larger (or shell thinner), the maximum of radial velocity will be reached closer to the crater edge and it will slightly decrease to the axis of symmetry. Note that initial rate of relaxation v_r (left panel of Figure 4.16) differs significantly for different thicknesses. See Figure 4.15 for relaxation curves for Models 6 – 8. We observe that for the same crater radii, the crater in the thickest shell relaxes the fastest.

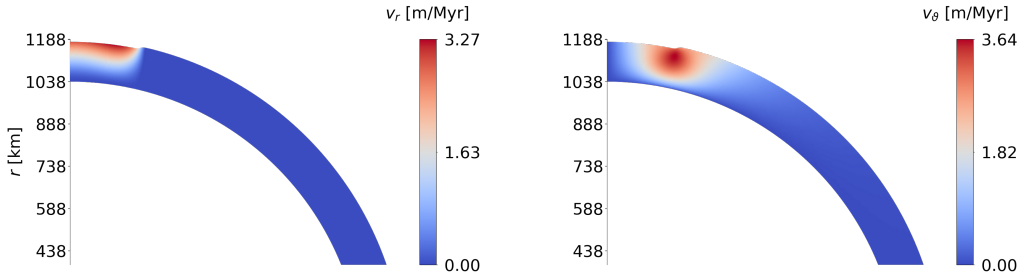

(a) $H = 150$ km.

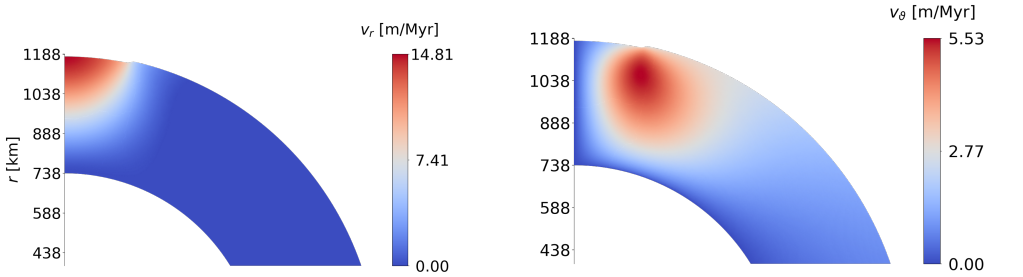

(b) $H = 450$ km.

Figure 4.16: Velocity profiles for Models 6 and 8. Left: radial component, right: lateral component. Note a significant difference in the radial velocity maximum.

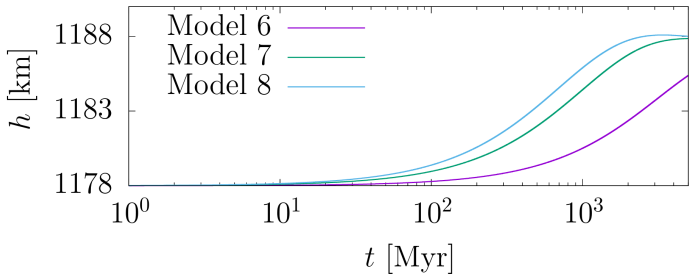

Figure 4.17: Relation curves for models 6 – 8.

This explains the situation in Figure 4.15. Crater with a diameter of 1000 km (Model 5) is noticeably wider than the shell thickness 327 km, therefore the fastest relaxation will not be at the axis of symmetry. We can see that Model 5 relaxes initially faster than Model 4 (crater diameter 500 km), however this is an effect of the temperature anomaly. Once the anomaly is cooled down ($\sim$ 700 Myr), the fastest region of relaxation moves from the axis of symmetry and the relaxation slows down.

5. Discussion and implications

Viscous relaxation of impact-deformed ice shell was shown to be a complex problem dependent on many parameters of the target ice body and the impactor. Here we discuss our results from Sections 4.2 and 4.3, and suggest possible ways for further research.

As we have expected, if Pluto's shell is made of ice only, the uplift relaxation would be rapid and the positive gravity anomaly cannot be maintained. Therefore, the shell reorientation would not be stable in long term. If the clathrate layer is present, stability can be substantially extended. Even though, by introducing impact heating and nonlinear ice and clathrates rheology, the stability does not exceed 1 Gyr, which differs from the conclusions of Kamata et al. [2019]

We have found out that ice shell and clathrate layer thickness are the crucial parameters determining the timescale of the relaxation. On the one hand, a thicker shell implies faster relaxation because of the $(R_o/R_i)^2$ dependence of the uplift height. Moreover, impact heating is more effective since the volume of warm ice increases with shell thickness. On the other hand, the thicker is the layer of clathrates, the cooler is the shell and the slower is the relaxation.

Models 10 and 11 (i.e. $H/h_c = 100/5$ km and 200/10 km, respectively) show how these parameters combine. Model 10 relaxes extremely slowly, even with only 5 km of clathrates. Because of the thin shell, the anomaly cools down quickly and the shell becomes cold and rigid. On the contrary, model 11 relaxes quickly, despite of double thickness of clathrates. Temperature anomaly is more stable in thick shell, which overpowers the former effect.

Still, there is one mechanism, which may speed up the relaxation even in the case of thin shell. The solid nitrogen layer, which accumulated in Sputnik Planitia basin, has thermal conductivity similar to clathrates ($0.7\ \mathrm{W \cdot m^{-1} \cdot K^{-1}}$) [Cook and Davey, 1976]. Once the nitrogen starts to accumulate, the shell will warm up, since the area of the basin will be cooled less effectively. Due to high ice thermal conductivity at surface temperature ($\sim 13\ \mathrm{W \cdot m^{-1} \cdot K^{-1}}$), this effect should be important. Unfortunately, the timescale of nitrogen accumulation is not known. So far, Hamilton et al. [2016] estimated millions or even billions of years based on Pluto's obliquity cycle.

Another questionable parameter is stability of the clathrate layer after the impact. The recent simulations of basin forming impact by Denton et al. [2020] showed that both the ice shell and the ocean beneath were ejected and the transient crater was filled by a mixture of crushed ice and water. It is therefore highly unlikely that the initial condition for uplift relaxation is a uniform undisrupted layer of clathrates, as Kamata et al. [2019] proposed. Therefore, it might be useful to implement clathrate layer evolution, which was suggested in Supplementary information of Kamata et al. [2019].

Parametric study of surface crater relaxation showed us the dependence of the relaxation timescale on the impactor radius. If the final crater radius is larger than the shell thickness, the relaxation will be slightly slower. If we want to investigate the relaxation of Sputnik Planitia basin, elasticity and plasticity should be taken into account. Similarly, the pressure of the nitrogen layer, which, in this case acts both as an thermal insulator and as a surface load, should be

taken into account. Again, it is not known when it started to accumulate and at what rate. Once the load reaches hydrostatic equilibrium with the basin, the relaxation stops. If this is the case, we cannot decide for how long the relaxation is over, therefore we may not be able to conclude anything about relaxation from the observed surface crater.

Conclusions

In this thesis, we investigated the viscous relaxation of Sputnik Planitia uplift with and without the clathrate layer proposed by Kamata et al. [2019] and surface crater relaxation for various impactor sizes and shell thicknesses.

Without the insulating and high viscosity layer of clathrates, the ocean uplift relaxes in less than 10 Myr for shells of thickness 100 – 200 km and gravity anomaly loses its positive sign even earlier. We further investigated the effect of a 5 – 10 km thick clathrate layer on a 150 km shell. Depending on the clathrate layer thickness, the relaxation timescale can be substantially prolonged: by two orders of magnitude for a 5 km layer, by 6 orders of magnitude for a 10 km layer.

We investigated two models for which Kamata et al. [2019] obtained relaxation times in the order of billions years. Due to the inclusion of the impact heating and nonlinear ice and clathrates rheology, the model with 200 km shell and with 10 km thick clathrate layer starts relaxing in 0.01 Myr, while the model with 100 km shell and 5 km thick clathrate layer starts relaxing around 1 Gyr. Both results thus differ from the conclusion of Kamata et al. [2019]. Moreover, the insulating effect of the accumulated nitrogen layer, as well as the unlikeliness of a uniform undisrupted clathrate layer, should be taken into account.

Models of a surface crater relaxation showed that relaxation timescale depends on the impactor radius (determining the final crater and isobaric core radii) and, for larger craters, on the shell thickness.

Our results suggest that the hypothesis by Kamata et al. [2019] might be sufficient to explain the reorientation, but not to explain the current orientation. However, although ocean uplift rises naturally in case of the impact, it cannot be excluded that the positive gravity anomaly is primarily being maintained by the impactor remnants, if it was denser than ice. The question of Pluto's ocean is therefore left for future studies. Data from future missions should help to answer this question.

Bibliography

G. B. Airy. On the computation of the effect of the attraction of mountain-masses, as disturbing the apparent astronomical latitude of stations in geodetic surveys. *Philosophical Transactions of the Royal Society of London*, 145:101–104, 1855. ISSN 02610523. URL `http://www.jstor.org/stable/108511`.

M. Alnæs, J. Blechta, J. Hake, A. Johansson, B. Kehlet, A. Logg, C. Richardson, J. Ring, M. E. Rognes, and G. N. Wells. The FEniCS Project Version 1.5. *Archive of Numerical Software*, 3, 2015. doi: 10.11588/ans.2015.100.20553.

Konstantin Batygin and Michael Brown. Evidence for a distant giant planet in the solar system. *The Astronomical Journal*, 151:22, 01 2016. doi: 10.3847/0004-6256/151/2/22.

Carver Bierson, F. Nimmo, and S. Stern. Evidence for a hot start and early ocean formation on Pluto. *Nature Geoscience*, 13, 07 2020. doi: 10.1038/s41561-020-0595-0.

Peter Buhler and Andrew Ingersoll. Sublimation pit distribution indicates convection cell surface velocities of ≈ 10 centimeters per year in Sputnik Planitia, Pluto. *Icarus*, 300, 09 2017. doi: 10.1016/j.icarus.2017.09.018.

Mathieu Choukroun, Susan Kieffer, Xinli Lu, and Gabriel Tobie. Clathrate hydrates: Implications for exchange processes in the outer solar system. *The Science of Solar System Ices*, pages 409–, 04 2013. doi: 10.1007/978-1-4614-3076-6_12.

T. Cook and G. Davey. The density and thermal conductivity of solid nitrogen and carbon dioxide. *Cryogenics*, 16(6):363–369, 1976. ISSN 0011-2275. doi: https://doi.org/10.1016/0011-2275(76)90217-4.

Lisandro Dalcín, Rodrigo Paz, and Mario Storti. MPI for Python. *Journal of Parallel and Distributed Computing*, 65(9):1108–1115, 2005. ISSN 0743-7315. doi: https://doi.org/10.1016/j.jpdc.2005.03.010. URL `https://www.sciencedirect.com/science/article/pii/S0743731505000560`.

C. Denton, Brandon Johnson, Shigeru Wakita, Andrew Freed, H. Melosh, and S. Stern. Pluto's Antipodal Terrains imply a thick subsurface ocean and hydrated core. *Geophysical Research Letters*, 48, 12 2020. doi: 10.1029/2020GL091596.

Jean Donea, Antonio Huerta, Jean-Philippe Ponthot, and Antonio Rodriguez-Ferran. *Arbitrary Lagrangian-Eulerian Methods*, volume 1, pages 413–437. 11 2004. ISBN 9780470091357. doi: 10.1002/0470091355.ecm009.

William Durham, Stephen Kirby, Laura Stern, and Wu Zhang. The strength and rheology of methane clathrate hydrate. *J. Geophys. Res*, 108, 04 2003. doi: 10.1029/2002JB001872.

Jouni Freund and Rolf Stenberg. On weakly imposed boundary conditions for second order problems. *Proceedings of the Ninth International Conference on Finite Elements in Fluids*, pages 327–336, 01 1995.

D. Goldsby and D. Kohlstedt. Superplastic deformation of ice: Experimental observations. *Journal of Geophysical Research: Solid Earth*, 106, 07 2001. doi: 10.1029/2000JB900336.

Sarah Greenstreet, Brett Gladman, and William McKinnon. Impact and cratering rates onto Pluto. *Icarus*, 258, 06 2015. doi: 10.1016/j.icarus.2015.05.026.

W. Grundy, Richard Binzel, B. Buratti, Jason Cook, D. Cruikshank, Cristina Dalle Ore, A. Earle, K. Ennico, C. Howett, Allen Lunsford, C. Olkin, A. Parker, Sylvain Philippe, Silvia Protopapa, Eric Quirico, Dennis Reuter, Bernard Schmitt, Kelsi Singer, A. Verbiscer, and Leslie Young. Surface compositions across pluto and charon. *Science*, 351:aad9189–aad9189, 03 2016. doi: 10.1126/science.aad9189.

Douglas Hamilton, S. Stern, J. Moore, and Leslie Young. The rapid formation of Sputnik Planitia early in Pluto's history. *Nature*, 540:97–99, 11 2016. doi: 10.1038/nature20586.

P.V. Hobbs. *Ice Physics*. Oxford Classic Texts in the Physical Sciences. OUP Oxford, 2010. ISBN 9780199587711.

D.L. Hogenboom, J.S. Kargel, J.P. Ganasan, and L. Lee. Magnesium sulfate-water to 400 mpa using a novel piezometer: Densities, phase equilibria, and planetological implications. *Icarus*, 115(2):258–277, 1995. ISSN 0019-1035. doi: https://doi.org/10.1006/icar.1995.1096. URL `https://www.sciencedirect.com/science/article/pii/S0019103585710962`.

B. C. Johnson, T. J. Bowling, A. J. Trowbridge, and A. M. Freed. Formation of the Sputnik Planum basin and the thickness of Pluto's subsurface ocean. *Geophysical Research Letters*, 43:10068–10077, 2016. doi: 10.1002/2016GL070694.

Mika Juntunen and Rolf Stenberg. Nitsche's method for general boundary conditions. *Mathematics of computation*, 78:1353–1374, 2009. doi: 10.1090/S0025-5718-08-02183-2.

Shunichi Kamata, F. Nimmo, Yasuhito Sekine, Kiyoshi Kuramoto, Naoki Noguchi, Jun Kimura, and Atsushi Tani. Pluto's ocean is capped and insulated by gas hydrates. *Nature Geoscience*, 12, 06 2019. doi: 10.1038/s41561-019-0369-8.

Boris J. P. Kaus, Hans Mühlhaus, and Dave A. May. A stabilization algorithm for geodynamic numerical simulations with a free surface. *Phys. Earth Planet. In.*, 181:12–20, 2010. doi: 10.1016/j.pepi.2010.04.007.

James Keane, Isamu Matsuyama, Shunichi Kamata, and Jordan Steckloff. Reorientation and faulting of Pluto due to volatile loading within Sputnik Planitia. *Nature*, 540, 11 2016. doi: 10.1038/nature20120.

Martin Kihoulou. Viscoelastic deformation of ice bodies in the solar system, 2019.

Heinz Kohnen. The temperature dependence of seismic waves in ice. *Journal of Glaciology*, 13(67):144–147, 1974. doi: 10.3189/S0022143000023467.

Anders Logg, Kent-Andre Mardal, and Garth Wells, editors. *Automated Solution of Differential Equations by the Finite Element Method*, volume 84 of *Lecture Notes in Computational Science and Engineering*. Springer-Verlag Berlin Heidelberg, 2012. doi: 10.1007/978-3-642-23099-8.

Zdeněk Martinec. Continuum Mechanics (Lecture Notes)., 2011. URL `http://geo.mff.cuni.cz/studium/Martinec-ContinuumMechanics.pdf`. Navštíveno dne 10. 4. 2019.

Isamu Matsuyama and F. Nimmo. Pluto's tectonic pattern predictions. pages 1399–, 03 2013.

Ctirad Matyska. Mathematical introduction to geothermics and geodynamics (Lecture Notes)., 2005. URL `http://geo.mff.cuni.cz/studium/Matyska-MathIntroToGeothermicsGeodynamics.pdf`. Visited 29. 4. 2021.

H. Jay Melosh. *Impact cratering*, page 222–275. Cambridge Planetary Science. Cambridge University Press, 2011. doi: 10.1017/CBO9780511977848.007.

J. Monteux, Nicolas Coltice, F. Dubuffet, and Yanick Ricard. Thermo-mechanical adjustment after impacts during planetary growth. *Geophysical Research Letters*, 34, 12 2007. doi: 10.1029/2007GL031635.

J. Monteux, Gaël Choblet, G. Tobie, and Mathieu Le Feuvre. Can large icy moons accrete undifferentiated? *Icarus*, 237:161–, 04 2014. doi: 10.1016/j.icarus.2014.04.041.

Jeffrey Moore, William McKinnon, John Spencer, Alan Howard, Paul Schenk, Ross Beyer, F. Nimmo, Kelsi Singer, Orkan Umurhan, Oliver White, S. Stern, Kimberly Ennico, C. Olkin, Harold Weaver, Leslie Young, Richard Binzel, Marc Buie, Bonnie Buratti, Andrew Cheng, and E. Zirnstein. The geology of pluto and charon through the eyes of new horizons. *Science*, 351:1284–1293, 03 2016. doi: 10.1126/science.aad7055.

COMSOL Multiphysics. Introduction to COMSOL Multiphysics®. *COMSOL Multiphysics, Burlington, MA, accessed Feb*, 9:2018, 1998.

NASA. True Colors of Pluto. [online], 2018. URL `https://solarsystem.nasa.gov/resources/933/true-colors-of-pluto/`. Johns Hopkins University Applied Physics Laboratory/Southwest Research Institute/Alex Parker.

NASA/JHUAPL/SwRI. A day on Pluto. [online], 2015. URL `https://www.nasa.gov/feature/a-day-on-pluto-a-day-on-charon/`.

NASA/JPL/Northwestern University. PIA02445: Hilly and Lineated Terrain. [online], 2000. URL `https://photojournal.jpl.nasa.gov/catalog/PIA02445`.

NASA/JPL/Northwestern University. PIA19213: The Mighty Caloris. [online], 2015. URL https://photojournal.jpl.nasa.gov/catalog/PIA19213.

F Nimmo and R Pappalardo. Ocean Worlds in the Outer Solar System. *Journal of Geophysical Research: Planets*, 121:1378–1399, 07 2016. doi: 10.1002/2016JE005081.

F. Nimmo, D. P. Hamilton, W. B. McKinnon, P. M. Schenk, R. P. Binzel, C. J. Bierson, R. A. Beyer, J. M. Moore, S. A. Stern, H. A. Weaver, C. B. Olkin, L. A. Young, and K. E. Smith. Reorientation of Sputnik Planitia implies a subsurface ocean on Pluto. *Nature*, 540:94–96, 2016a. doi: 10.1038/nature20148.

F. Nimmo, Orkan Umurhan, Carey Lisse, Carver Bierson, Tod Lauer, Marc Buie, Henry Throop, Josh Kammer, James Roberts, William McKinnon, Jeffrey Moore, S Stern, Leslie Young, Harold Weaver, C. Olkin, Kim Ennico, and the team. Mean radius and shape of Pluto and Charon from New Horizons images. *Icarus*, 287, 03 2016b. doi: 10.1016/j.icarus.2016.06.027.

A. Quarteroni and A. Valli. *Numerical Approximation of Partial Differential Equations*. Springer Series in Computational Mathematics. Springer-Verlag Berlin Heidelberg, 1994. ISBN 978-3-540-85268-1. doi: 10.1007/978-3-540-85268-1.

Rishi Raj and M. Ashby. On grain boundary sliding and diffusional creep. *Metallurgical Transactions*, 2:1113–1127, 04 1971. doi: 10.1007/BF02664244.

G. Robuchon and F. Nimmo. Thermal evolution of Pluto and implications for surface tectonics and a subsurface ocean. *Icarus*, 216:426–439, 12 2011. doi: 10.1016/j.icarus.2011.08.015.

Guglielmo Scovazzi and Thomas J. R. Hughes. Lecture Notes on Continuum Mechanics on Arbitrary Moving Domains. Sandia National Laboratories, 11 2007.

Myles Standish. Planet X - No dynamical evidence in the optical observations. *The Astronomical Journal*, 105, 06 1993. doi: 10.1086/116575.

A. Stern, L. Trafton, M. Buie, W. Grundy, and L. E. Young. Hubble maps Pluto's changing surface. [online], 2010. URL https://hubblesite.org/contents/media/images/2010/06/2687-Image.html?news=true.

C. Taylor and P. Hood. A numerical solution of the Navier-Stokes equations using the finite element technique. *Computers and Fluids*, 1(1):73 – 100, 1973. doi: 10.1016/0045-7930(73)90027-3.

Gabriel Tobie, O. Grasset, Jonathan Lunine, Antoine Mocquet, and Christophe Sotin. Titan's internal structure inferred from a coupled thermal-orbital model. *Icarus*, 175:496–502, 06 2005. doi: 10.1016/j.icarus.2004.12.007.

Alexander Trowbridge, Jay Melosh, Jordan Steckloff, and A. Freed. Vigorous convection as the explanation for Pluto's polygonal terrain. *Nature*, 534:79–81, 06 2016. doi: 10.1038/nature18016.

W. Waite, L. Stern, Stephen Kirby, W. Winters, and D. Mason. Simultaneous determination of thermal conductivity, thermal diffusivity and specific heat in sI methane hydrate. *Geophysical Journal International*, 169, 12 2006. doi: 10.1111/j.1365-246X.2007.03382.x.

Kevin Zahnle, Paul Schenk, Harold Levison, and Luke Dones. Cratering rates in the outer solar system. *Icarus*, 163:263–289, 02 2003. doi: 10.1016/S0019-1035(03)00048-4.

List of Figures